Funded by the
European Union

Compact

Ref. Ares(2019)6470165 - 19/10/2019

XLS-Report-2019-002
27 June 2019

XLS Deliverable D3.2

Review report on bunch compression techniques and phase space linearization

J.M. Arnesano[||], M. Croia[‡], S,. Di Mitri[1)*],
L. Ficcadenti[**], A. Faus-Golfe[§], A. Giribono[‡], Y. Han[§],
A. Latina[†], X. Liu[†], E. Marin Lacoma[¶],
R. Muñoz Horta[¶], A. Mostacci[||], L. Palumbo[||],
B. Spataro[‡], C. Vaccarezza[‡]

On behalf of the CompactLight Partnership

Prepared on: 27.06.2019

[*] Sincrotrone Trieste, Italy, [†] CERN, Switzerland, [‡] INFN-LNF, Italy, [§] LAL, France,
[¶] ALBA-CELLS Synchrotron, Spain, [||] Univ. of Rome La Sapienza, Italy, [**] INFN-Roma, Italy

[1]Corresponding author: simone.dimitri@elettra.eu

Funded by the
European Union

Compact

This project is funded by the European Union's Horizon2020 research and innovation programme under Grant Agreement No. 777431. The contents of this report reflect only the view of the CompactLight Consortium. The European Commission is not responsible for any use that may be made of the information it contains.

Abstract

This document describes with analytical and numerical methods, i.e., approximated mathematical expressions and particle tracking runs, the process of bunch length compression of relativistic electron beams in linear accelerators. In particular, it reviews state-of-the-art compression options, based on magnetic insertions and radio-frequency (RF) accelerators, for the increase of peak current and preservation of the six-dimensional beam brightness as requested by x-ray free-electron lasers (FELs). After a theoretical introduction to the topic, guidelines for the determination of the compression scheme for the CompactLight FEL are provided, by considering for example RF compression in combination with four dipoles chicanes. The study considers single particle dynamics, tolerance budget and collective effects involved in the compression process. On the basis of FEL specifications, the main parameters of the electron beam and of the compressors in the CompactLight accelerator are illustrated. Finally, a preliminary RF design of X-band and Ka-band accelerating cavities to support magnetic compression is presented. As a result, this review of most advanced electron beam compression schemes provides a solid basis for the definition of the beam manipulation aimed to meet the requirements of CompactLight FEL.

Contents

1 Theoretical Background **5**
1.1 Motivations . . . 5
1.2 Basics of Magnetic Compression . . . 5
1.3 RF Linearization . . . 8
1.4 Passive Linearization . . . 9
1.5 Magnetic Compressor Geometries . . . 11
1.6 Jitter Budget . . . 12
1.7 RF Bunching . . . 13

2 Determination of the Compression Scheme for CompactLight **15**
2.1 Choice of RF compression . . . 15
2.2 Choice of Injector RF frequency . . . 16
2.3 Choice of magnetic compressor geometry . . . 19

3 CompactLight FEL Working Point **20**
3.1 Electron Beam Parameters . . . 20
3.2 Compressor Parameters vs. Bunch Length . . . 21
3.3 Compressor Parameters vs. Beam Emittance . . . 22
3.4 One-Dimensional Particle Tracking . . . 24
3.5 Sensitivity and tolerance study . . . 28
3.6 Coherent Synchrotron Radiation . . . 29
3.7 Options for minimization of CSR effects . . . 33

4 Preliminary RF design **36**
4.1 X-band linearizer . . . 36
4.1.1 Single Cell design . . . 37
4.1.2 Coupler Design . . . 38
4.1.3 Full Structure EM Simulation and Breakdown Analysis . . . 40
4.2 Ka-band linearizer . . . 41
4.2.1 Choice of the structure parameters . . . 43
4.2.2 Accelerating structure RF properties . . . 44
4.2.3 Breakdown rate (BDR) limit . . . 45
4.2.4 Thermal and Stress Analysis . . . 48
4.2.5 Ka-band linearizer main parameters . . . 48

1 Theoretical Background

1.1 Motivations

There is a growing demand for generating and accelerating very short, high charge density electron bunches for high gain soft and hard X-ray free-electron lasers (FELs). The generation of hundreds of amperes peak current electron bunches directly out of an electron source is in conflict with the production of small transverse emittance beams, due to the repulsive inter-particle Coulomb interactions ('space-charge' forces) that are especially effective at low beam energies. It is therefore preferable to create only a few tens of amperes-peak current bunches at the source, such as an RF photo-injector, in order to dilute the charge density, and thereby ensure small transverse emittances. Beam manipulations are implemented then in the downstream transport line, at higher beam energies, in order to obtain short electron bunches while preserving the normalized emittance at the injector level. The process of manipulating an electron beam so to enhance its peak current is called, in short, bunch compression.

1.2 Basics of Magnetic Compression

We consider the motion of ultra-relativistic particles in an RF linac made, for example, of copper structures with inner irises. We assume each structure made of identical cylindrical cells; the RF power flows through the cells, and is eventually extracted on a load. Such structures behave like waveguides of cylindrical symmetry, and the longitudinal electric field component, which has in general a radial dependence, is a superposition of *n* field harmonics characterized by an angular RF frequency ω and by an RF wave-number *k*:

$$\begin{aligned} E_z^{TW} &= \sum_{n=-\infty}^{+\infty} a_n J_n(k_{r,n} r)\cos(\omega t(z) - k_n s + \varphi) \cong E_{z,0}^{TW}\cos(\omega t_{syn} + \omega\Delta t - ks + \varphi) \\ &= E_{z,0}^{TW}\cos(\omega t_{syn} - ks + \varphi + kz) \equiv E_{z,0}^{TW}\cos(\phi_{rf} + kz), \end{aligned} \tag{1}$$

where the generic particle time coordinate $t(z)$ was expanded in the arrival time t_syn of the reference (or synchronous) particle, e.g. the bunch centroid, plus the arrival time of the generic particle with respect to it. We then used the identity $\omega\Delta t = kz$. The z-coordinate runs inside the bunch, with z = 0 for the reference particle. The s-coordinate runs along the electric axis of the cell. The arbitrary phase φ determines the arrival time of the reference particle relative with respect to the electric field inside the cell. Finally, we defined the RF phase $\phi_{rf} = \omega t_{syn} - ks + \varphi$, which tends to be constant for ultra-relativistic beams.

The last term of Eq. 1 describes the fundamental on-axis mode of the longitudinal electric field in a 'travelling wave' (TW) accelerating structure. In fact, we assume that the transverse beam sizes are much smaller than the structure inner radius, and that the beam is well centered on the structure's electric axis. Moreover, most of the acceleration is provided by the fundamental mode of the field. We keep the notation according to which beam acceleration (i.e., acceleration sampled by the reference particle) is maximum for $\phi_{rf} = 0$: in this case the beam is said to be 'on-crest' of the RF wave. As we will see in the next section, magnetic bunch-length compression requires a correlation of the particles' energy with their longitudinal positions inside the bunch, and such a correlation is established by operating the linac 'off-crest', namely at an RF phase $-\pi < \phi_{rf} < 0$ or $0 < \phi_{rf} < \pi$, depending on the geometry of the downstream magnetic insertion. The special point $\phi_{rf} = \pm\pi/2$ is commonly called 'zero

crossing'. Accelerated either on-crest or off-crest, we assume here that the beam longitudinal phase space (z, E) is mainly determined by the curvature imposed by the cosine-like behaviour of the accelerating field.

The coefficient used to quantify the linear correlation in (z, E) is named 'linear energy chirp', and it can be evaluated by expanding the electric field-induced energy gain to first order in z:

$$h \equiv \frac{1}{E_0}\frac{\mathrm{d}E}{\mathrm{d}z} \cong \frac{1}{E_i + e\Delta V_0 \cos\phi_{rf}}\frac{\mathrm{d}}{\mathrm{d}z}[E_i + e\Delta V_0\cos(\phi_{rf}) - e\Delta V_0 kz\sin(\phi_{rf}) + o(z^2)] \\ = -\frac{e\Delta V_0 k\sin\phi_{rf}}{E_i + e\Delta V_0\cos\phi_{rf}} \tag{2}$$

where the beam is injected into the linac with a mean energy E_i. When the beam energy spread induced by the RF curvature is much larger than the uncorrelated energy spread, which depends on the process of beam generation, we may estimate $|h| \approx \sigma_\delta/\sigma_z$. As a consequence, as long as the beam correlated energy spread is constant when the bunch length is shortened (or lengthened) in a magnetic insertion, the energy chirp is increased (or lowered) by the same compression factor.

Particles with different longitudinal momentum will follow different (longer vs. shorter) orbits in dipole magnets. Since the longitudinal velocity of all particles is assumed to be very close to c independently from their spread in energy, the particles will arrive at a longitudinal position s downstream of the magnet at different times. In other words, the longitudinal coordinate z of particles inside the bunch is changed. We therefore envision a way to shorten or lengthen the bunch, with a suitable arrangement of energy spread and dipole magnets. The former is manipulated with an RF linac as depicted in the previous section. In particular, the energy spread is correlated along the bunch so that, for example, less energetic particles in the bunch head will follow orbits longer than more energetic particles in the bunch tail, as shown in Fig. 1. At the exit of the magnetic insertion, the bunch head and tail will have been caught towards the bunch centre, and the bunch length will be shortened.

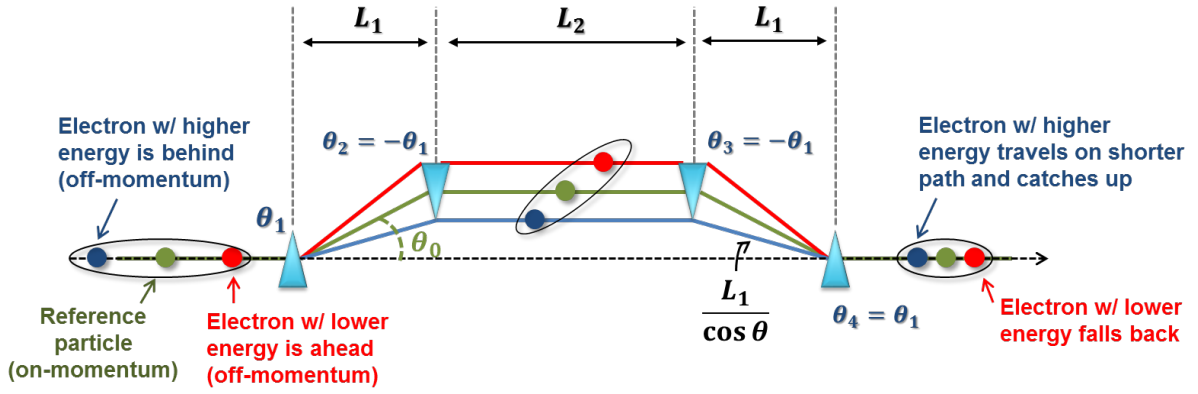

Figure 1: Geometry (not to scale) of a four-dipole symmetric magnetic chicane, and particles' motion through it for the case of bunch-length compression.

In accelerator physics, the evolution of particle 6D coordinates through an arbitrary beam line is commonly depicted through the matrix formalism, i.e., each element of the beam line is depicted through a matrix whose terms depend on the element's parameters and geometry. A beam line made of consecutive elements is represented by a matrix that is the ordered

product of the individual ones. Thus, the dependence of a particle's z-coordinate at the exit of the chicane on its momentum deviation can be written as $z_f(\delta) = z_i + R_{56}\delta$, with R_{56} the chicane matrix element. When the path length in non-zero-length dipoles is included, we have:

$$R_{56} \cong -2\theta_0^2(L_1 + \frac{2}{3}l_d) \tag{3}$$

More accurate expressions, which typically give small corrections to Eq. 3, can be found in the literature [1].

We differentiate the particle longitudinal slippage, evaluated through the whole chicane, and keep only terms to first order in the particle coordinates (linear approximation):

$$\begin{aligned} \mathrm{d}z_f = \mathrm{d}z_i + R_{56}\mathrm{d}\delta &\cong \mathrm{d}z_i + R_{56}\frac{\mathrm{d}E}{E_0} \\ &= \mathrm{d}z_i\left(1 + R_{56}\frac{1}{E_0}\frac{\mathrm{d}E(z)}{\mathrm{d}z_i}\right) + R_{56}\frac{\mathrm{d}E_{unc}}{E_0} \\ &= \mathrm{d}z_i\,(1 + h_i R_{56}) + R_{56}\delta_{unc} \\ &\equiv \mathrm{d}z_i/C + R_{56}\delta_{unc} \end{aligned} \tag{4}$$

z is the electron beam mean energy at the compressor and δ is the energy deviation relative to z. We have split the particle energy deviation into two terms, one for the energy deviation correlated with z, which translates into the initial linear energy chirp h_i, and the other one for the initial uncorrelated energy deviation, δ_{unc}. Eq. 4 1.2.5 defines the *linear* compression factor $C = (1 + h_i R_{56}) - 1$. It is worth noticing that $C \to \infty$ for $R_{56} = -1/H_i$. However, even in that limit, the actual bunch length is finite and reaches the minimum rms value $\sigma_{z,\min} = R_{56}\sigma_{\delta,unc}$ by virtue of a non-zero δ_{unc}. Thus, 'full' compression at higher beam energies would result in shorter minimum bunch lengths. With accepted convention, the chicane geometry in Fig. 1 provides $R_{56} < 0$, and therefore the bunch length is shortened if $h_i > 0$, namely if the bunch head has a lower energy than the bunch tail. If a non-linear energy chirp is present (E depends on z at higher orders in z), we expect $h_i(z)$ to vary along the bunch, and so will C.

We write down the total relative energy spread of a generic particle as the sum of an uncorrelated term (δ_u) and a z-correlated term (δ_c), the latter being the beam energy chirp times the particle z-position. The total energy spread is assumed constant through the chicane (only magnetic fields are involved, and no frictional forces), and the final bunch length is expressed as a function of the initial one through the definition of C given above:

$$\begin{aligned} \delta_{tot} &= \delta_{u,i} + \delta_{c,i} \\ &= \delta_{u,i} + h_i\Delta z_i \\ &\equiv \delta_{u,f} + h_f\Delta z_f \\ = \ldots &= \delta_{u,f} + Ch_i\left(\frac{\Delta z_i}{C} + R_{56}\delta_{u,i}\right) + o(\delta^2, \Delta z^2) \end{aligned} \tag{5}$$

By equating the third and the last terms of Eq. 5, and then passing to the rms value of the quantities, we find:

$$\sigma_{u,f}^2 = \sigma_{u,i}^2(1 - Ch_i R_{56})^2 = C^2\sigma_{u,i}^2 \tag{6}$$

i.e., the uncorrelated energy spread is increased by the same factor C by which the bunch length is shortened.

1.3 RF Linearization

Quadratic and even cubic components of the energy chirp may play an important role in the compression process, as C is no longer constant through the bunch, and different longitudinal portions of the bunch (slices) may be compressed in a different manner. Such a dynamics would imply that the current profile before compression is not preserved by the compression process. The situation is additionally deteriorated by a higher order dispersion function that translates into a higher order momentum compaction (T_{566} term at second order, U_{5666} at third order, etc.). In order to evaluate such a non-linear dynamics, we start expanding the expression for the energy gained by a generic particle in an RF linac to second order in z. For illustration, we ignore at this stage the second-order momentum compaction in the chicane. We find:

$$E_1 \cong E_i + e\Delta V_0 \cos\phi_{rf} - e\Delta V_0 kz \sin\phi_{rf} - \frac{e\Delta V_0}{2} k^2 z^2 \cos\phi_{rf} + o(z^3). \tag{7}$$

The second-order term in z can be cancelled by means of an additional RF component, but with different RF wavenumber:

$$\begin{aligned} E_2 &= E_1 + e\Delta V_H \cos(k_H z + \phi_H) \\ &\cong E_1 + e\Delta V_H \cos\phi_H - e\Delta V_H k_H z \sin\phi_H - \frac{e\Delta V_H}{2} k_H^2 z^2 \cos\phi_H + o(z^3). \end{aligned} \tag{8}$$

By comparing Eq.7 and Eq.8, we find that the quadratic term generated by the additional structure(s) has to be positive, i.e., $\cos\phi_H$(say, $\phi_H = \pi$) and therefore the zeroth-order term from the additional linac is *decelerating* the beam. The new linac voltage has to satisfy $\Delta V_H = \frac{k^2}{k_H^2}\Delta V_0 \cos\phi_{rf}$. Thus, compensation of the second-order energy chirp ('RF curvature') and net beam acceleration can only be achieved simultaneously if the RF wavenumber of the additional linac (often named 'linearizer') is larger than the one of the baseline accelerator. The scaling of the linearizer peak voltage with the wavenumber favours this approach, as long as the ratio of wavenumbers is 1/3 or smaller. For example, a baseline RF linac running in the S-band 3 GHz RF and providing 200 MeV energy gain can be supplied by an additional X-band 12 GHz RF structure with peak voltage at ~ 15 MV level.

In a more complete analysis, the particle energy deviation combines with the expression for the energy chirp up to second order. In this more general and realistic case, linearization does not apply to the longitudinal phase space at the entrance of the chicane only, but to the compression process as a whole, through the RF linac *and* the chicane. By imposing that the beam mean energy at the chicane, E_{BC}, and the final bunch length do not change w.r.t. the case of purely linear motion, and additionally ignoring the contribution of the uncorrelated energy spread to the final bunch length, we find the peak voltage of the harmonic cavity required for linearization:

$$e\Delta V_H = \frac{1}{\left(k_H^2/k^2 - 1\right)} \left\{ E_{BC} \left[1 + \frac{2}{k^2} \frac{T_{566}}{|R_{56}|^2} \left(1 - \frac{1}{C} \right)^3 \right] - E_i \right\} \tag{9}$$

Although Eq. 9 is valid for a one-stage compression only, the dependence of the linearizer peak voltage on the RF wavenumber is the same for multistage compression schemes. Moreover, when two chicanes or more are adopted, the peak-voltage setting does not vary much because after the first chicane the bunch is shorter and less vulnerable to RF curvature.

Alternative methods for the linearization of the compression process include passive dielectric-lined insertions or magnetic elements. In the former case, an optimum longitudinal voltage

loss over the length of the bunch can be provided in order to compensate both the second-order RF time curvature and the second-order momentum compaction term. This technique is discussed at the end of this Section. Removal of second-order nonlinearities in the longitudinal phase space through optical elements is typically dealt with by sextupole magnets. Sextupoles introduce a quadratic dependence of the particle path-length difference on energy deviation through an effective T_{566} term that, if supplied with the appropriate sign, 'stretches' the curvature in phase space. However, if the beam has to enter the undulator chain for lasing, tight tolerances on the final beam transverse emittance, both slice and projected, make the sextupole correction in a four-dipole chicane less attractive due to possible high-order magnetic aberrations. Moreover, the use of a higher-harmonic RF field does not introduce coupling between longitudinal and transverse phase-space coordinates, unlike optical manipulation of R_{56} and T_{566} terms does. For this reason, to date most of the FEL facilities have chosen to linearize the magnetic compression process with up-frequency RF structures. In principle, sextupole-induced aberrations can be counteracted with a suitable betatron phase advance between those magnets. This approach, however, implies a more sophisticated design of the chicane or a different geometry of the magnetic compressor [2, 3]. It is worth noticing that a larger T_{566} term, such as the one provided by a multistage compression scheme, may be helpful in the reduction of the quadratic energy chirp induced by longitudinal geometric wake fields excited in small-iris accelerating structures. The multistage compression, however, tends to amplify the so-called microbunching instability, which implies a finally increased energy spread and modulated current profile, as discussed in the next chapter.

1.4 Passive Linearization

The longtidinal wakefield for a dielectric waveguide can be expressed as:

$$w_{||}(z) = A\cos(k_s z) \tag{10}$$

Here A is the amplitude for the wakefield. For a circular structure $A = \frac{Z_0 c}{\pi a^2}$, with $Z_0 = 377\ \Omega$ the impedance of free space and a the radius of the structure. For a rectangular structure, $A = \frac{\pi^2}{16}\frac{Z_0 c}{\pi a^2}$, with a the aperture of the structure. k_s is the wave number of the wakefield. For circular dielectric structure, $k_s = \sqrt{\frac{2\varepsilon}{a\delta(\varepsilon-1)}}$), with ε denote the relative permittivity, δ denote the thickness of the dielectric material. For circular corrugated structure, $k_s = \sqrt{\frac{2p}{a\delta g}}$, here p denote the corrugation period, δ denote the depth and g denote the gap width. For rectangular corrugated structure, $k_s = \sqrt{\frac{p}{a\delta g}}$.

For a bunch of beam, the wake potential is calculated as:

$$W(z) = -\int_{-\infty}^{z} w_{||}(z-z')\rho(z')dz' \tag{11}$$

Then the energy change due to the wake field is:

$$\Delta E(z) = -eLW(z) \tag{12}$$

If we consider a rectangular bunch distribution with fullwidth L_b, total charge Q, and distributed symmetrically about z=0, the energy change within this bunch due to the wakefield can be given by [4]:

$$\Delta E(z) = -\frac{eQLA}{k_s L_b}\sin(k_s z + \frac{k_s L_b}{2}) \tag{13}$$

If this electron beam passes through one linac segment and then through a passive structure. If the beam has an initial mean energy E_i, then following the linac and after the round pipe the electron energy for particles with $|z_0| \leq \frac{L_b}{2}$ is:

$$E(z_0) = E_i + eV_1 \cos(k_1 z_0 + \phi_1) + eA_s \sin(k_s z_0 + \phi_s) \tag{14}$$

Where k_1 is is the RF wave number, V_1 is the amplitude of the voltage of the linac segment, z_0 is the longitudinal position of the particle with respect to the bunch center, $A_s = \frac{QLA_0}{k_s L_b}$, and $\phi = k_s L_b/2$. When $\phi = \pi/2$, the passive structure can provide a decelerating voltage. This can be obtained with $k = \pi/L_b$. The relative energy deviation can be expanded in a power series about the reference particle and becomes:

$$\begin{aligned}
\Delta E(z_0)/E_0 \approx & -\frac{eV_1 k_1 \sin(\phi_1) + eA_s k_s \cos(\phi)}{E_0} z_0 \\
& -\frac{eV_1 k_1^2 \cos(\phi_1) - eA_s k_s^2 \sin(\phi)}{E_0} z_0^2 \\
& +\frac{eA_s k_s^3 \cos(\phi)}{6E_0} z_0^3 - \frac{eA_s k_s^4 \sin(\phi)}{24E_0} z_0^4 \\
= & az_0 + bz_0^2 + cz_0^3 + dz_0^4
\end{aligned} \tag{15}$$

Where E_0 is the chicane energy. The energy change due to the dielectric wakefield is expanded to fourth order, and the change due to RF linac is expanded to second order with assuming $k_1 L_b \ll 1$.

The magnetic chicane transformation can be written to third order like:

$$z = z_0 + R_{56}\Delta E/E_0 + T_{566}(\Delta E/E_0)^2 + U_{5666}(\Delta E/E_0)^3 \tag{16}$$

Where $T_{566} \approx -3R_{56}/2$ and $U_{5666} \approx 2R_{56}$ for a typical D-type chicane. Combined with the formulae above, we can get:

$$\begin{aligned}
z = & (1 + aR_{56})z_0 + (bR_{56} + a^2 T_{566})z_0^2 + (2abT_{566} + a^3 U_{5666} + cR_{56})z_0^3 \\
& + (dR_{56} + b^2 T_{566} + 3a^2 bU_{5666} + 2acT_{566})z_0^4 \\
& + (3a^2 cU_{5666} + 3ab^2 U_{5666} + 2adT_{566} + 2bcT_{566})z_0^5 \\
& + (3a^2 dU_{5666} + 6abcU_{5666} + b^3 U_{5666} + 2bdT_{566} + c^2 T_{566})z_0^6 \\
& + (3b^2 cU_{5666} + 6abdU_{5666} + 3ac^2 U_{5666} + 2cdT_{566})z_0^7 \\
& + (3b^2 dU_{5666} + 3bc^2 U_{5666} + 6acdU_{5666} + d^2 T_{566})z_0^8 \\
& + (c^3 U_{5666} + 6bcdU_{5666} + 3ad^2 U_{5666})z_0^9 \\
& + (3c^2 dU_{5666} + 3bd^2 U_{5666})z_0^{10} + (3cd^2 U_{5666})z_0^{11} + (d^3 U_{5666})z_0^{12}.
\end{aligned} \tag{17}$$

Fixing $k_1 z_0 \ll 1$, $k_1 \ll k_s$, $\phi \sim \pi/2$, $eV_1 \sim E_0$ and $QLA \ll E_0$, this formulae can be simplified as:

$$z \approx (1 + aR_{56})z_0 + (bR_{56} + a^2 T_{566})z_0^2 + dR_{56} z_0^4. \tag{18}$$

Then in order to compensate the quadratic term, the second order term must be set to zero. Then we have:

$$b = -T_{566}/R_{56}a^2 \approx 3/2a^2 \tag{19}$$

If the reference energy of the bunch is fixed at E_0, then the voltage of the linac have been increase in order to compensate the energy loss in the passive structure:

$$eV_1\cos(\phi_1) = E_0 - E_i + eA_s\sin(\phi_s) \tag{20}$$

Using this $eV_1\cos(\phi_1)$, the A_s needed to compensate the second order term can be expressed as:

$$A_s = \frac{1}{e\sin\phi_s x}\frac{k_1^2\left[E_0(1+3a^2/k_1^2) - E_i\right]}{k_s^2 - k_1^2} \tag{21}$$

Then the amplitude of the passive structure is:

$$A = \frac{L_b}{k_s}\frac{k_1^2\left[E_0(1+3a^2/k_1^2) - E_i\right]}{eQL} \tag{22}$$

Here we use $k_s \gg k_1$ and $\sin(\phi_s) \approx 1$.

In order to limit the effect of fourth order term, it is required that the fourth order term is much smaller than the liner term, which leads:

$$|R_{56}/(1+aR_{56})| \ll \frac{192E_0}{\pi^2 L_b k_1^2\left[E_0(1+3a^2/k_1^2) - E_i\right]} \tag{23}$$

1.5 Magnetic Compressor Geometries

Most common geometries of magnetic insertions for bunch-length compression are shown in Fig. 2. C-shape symmetric chicanes are very common because they allow remote control of the bending angle through a translation stage of the inner dipoles, for a tuning of the compression factor and balance of momentum compaction vs. coherent synchrotron radiation (CSR) instability, which is discussed in the next chapter. The inner drift section does not contribute to compression, but it offers room for hosting beam diagnostics and scrapers or masks for beam shaping. The chicane lateral arms may host weak quadrupole magnets for the correction of the spurious dispersion function due to dipole magnet errors. Different geometries (S-shape, asymmetric tuneable C-shape and double C-shape) of the chicane have been explored in literature and in existing facilities in order to minimize the impact of CSR emission on the beam emittance.

In symmetric C-shape geometries, all dipoles provide the same bending angle. For any given $R_{56} \cong -2\theta_0^2(L_1 + \frac{2}{3}l_d)$, we have $T_{566} \cong -1.5 \times R_{56}$, $U_{5666} \cong 2 \times R_{56}$. For compactness, the inner dipoles can be collapsed into one magnet with double bending angle than the outer ones. In S-shape geometries, the inner dipoles provide a bending angle larger than the outer ones. Quadrupole and sextupole magnets can interleave dipole magnets.

Arcs usually provide an R_{56} term with sign opposite to that of four-dipole chicanes, and are a natural choice for compression in recirculating machines, such as energy-recovery linacs. They may offer the chance of accommodating sextupole magnets for the linearization of the compression process, with a phase advance suitable for the cancellation of geometric and

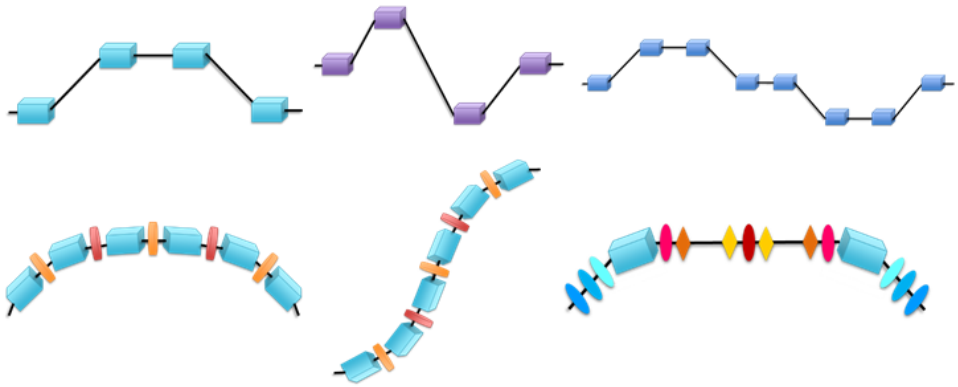

Figure 2: Most common geometries (not to scale) of magnetic insertions for bunch-length compression. From top, left to right: C-shape, S-shape and double C-shape chicanes; bottom, arc-fodo, dog-leg-fodo and double-bend achromat cell.

chromatic aberrations (the latter ones commonly dominate because of the relatively large relative energy spread required for compression). However, additional constraints on the linear optics functions in the bending plane are required in the arcs in order to minimize or cancel the otherwise CSR-induced projected emittance growth. An arc composed of N_c fodo cells (focusing and defocusing quadrupoles alternate, interleaved by identical dipoles), with betatron phase advance μ_x per cell in the bending plane, and extending over a total length L_arc, is characterized by $R_{56} \cong \frac{\theta_0^2 L_{arc}}{4N_c^2} \sin^2(\mu_x/2)$; with no sextupoles included typically $T_{566} \approx 2 \times R_{56}$ or larger. A dog-leg can be built with two consecutive arc-fodos. For the simplest two-dipole symmetric geometry, the dog-leg features $R_{56} \cong \theta_0^2 l_d/3$. A series of double- or multibend achromat cells can be used to build up an arc of arbitrary bending angle. In a periodic arc made of N_c identical symmetric double-bend achromatic cells, $R_{56} \cong 2N_c\theta_0^2 l_d$.

1.6 Jitter Budget

FELs usually require tight control of the electron-beam arrival time at the undulator. The shot-to-shot reproducibility of the arrival time of consecutive electron bunches, henceforth named 'arrival time jitter' (ATJ), is of great importance for multi-shot experiments. On the single-pulse basis, it is even more important for FELs driven by an external laser (externally seeded FELs), in order to ensure synchronism between the laser and the electron bunch. The requirement of small ATJ is particularly stringent when the electron bunch is longitudinally compressed to sub-ps durations, in order for the jitter to be (much) smaller than the bunch duration. We introduce a model for the ATJ in the presence of magnetic compression in a four-dipole chicane. The error sources contributing to the ATJ we consider are: photo-injector laser arrival time on the cathode, jitter of phases and voltages of the RF linac, and fluctuations of the compressor's dipole field, as they may be produced by fluctuations of the power converters.

We adopt the bunch centroid as the reference particle. Its final time coordinate in the laboratory frame is $t_f = t_i + \frac{\Delta l + L}{c}$, where t_i is the reference initial arrival time, L is the straight trajectory length through the chicane (zero bending angle) and $Delta$ is the path-length difference between the beam trajectory through the chicane with dipoles turned on and the straight trajectory. If $\theta << 1$, one finds $\Delta l \cong -R_{56}/2$. The rms ATJ after the beam has passed through

an RF linac and one chicane, where that all the jitter sources are assumed to be small and independent perturbations to the particles' motion, is:

$$\sigma_{t,f}^2 \cong \left(\frac{\sigma_{t,i}}{C}\right)^2 + \left(\frac{R_{56}}{c}\right)^2 \left[\left(\frac{eV\cos\phi}{E}\right)^2 \left(\frac{\sigma_V}{V}\right)^2 + \left(\frac{eV\sin\phi}{E}\right)^2 \sigma_\phi^2 + \left(\frac{\sigma_B}{B}\right)^2\right] \tag{24}$$

If no additional dispersive insertions are foreseen between the chicane and the undulator, the ATJ at the exit of the chicane will be frozen up to the end of the beam line. Reduction of the ATJ at the entrance of the chicane by the compression factor is due to the fact that an earlier (later) arrival of the bunch centroid to the RF field in the upstream linac translates, e.g., to a lower (higher) energy at the chicane, and therefore to a shorter (longer) path length with respect to the reference trajectory.

The linac peak voltage jitter maximally (minimally) contributes to the ATJ for the linac operated on crest (at zero-crossing). For on-crest operation, the RF phase jitter term can usually be neglected as long as the bunch length is much shorter than the RF wavelength. This 'out of phase' behaviour of the two RF jitter sources suggests the possibility of choosing the RF linac phase in a way that, for any specified error budget, the ATJ is minimum. Although quite an attractive option in principle, such an optimal linac configuration constrains the compression factor to some specific values or to a limited range, for any given setting of the magnetic chicane. In the case of multistage compression schemes, more RF settings are available that may simultaneously ensure the lowest ATJ for a design compression factor, energy spread and chicane bending angle.

A jitter of the compression factor implies a jitter of the final bunch length or of the final peak current, for initially constant bunch length and bunch charge, respectively. We anticipate that, owing to the fact that the linac upstream of the chicane is run off-crest in practical cases, the jitter of C is dominated by the RF phase jitter. We therefore differentiate the expression for C assuming that only the RF phase varies (namely, we neglect any variation of linac peak voltage and dipole field):

$$\begin{aligned} \Delta\left(\frac{1}{C}\right) = -\frac{\Delta C}{C^2} = \Delta(1+hR_{56}) \cong R_{56}\frac{\Delta h}{H}h \cong R_{56}\frac{\Delta(\sin\phi)}{\sin\phi}h = hR_{56}\frac{\Delta\phi}{\tan\phi}, \\ \frac{\Delta C}{C} \cong -ChR_{56}\frac{\Delta\phi}{\tan\phi} = (C-1)\frac{\Delta\phi}{\tan\phi}, \\ \sigma_C^2 \cong (C-1)^2\frac{\sigma_\phi^2}{\tan^2\phi}. \end{aligned} \tag{25}$$

The *relative* jitter of C is proportional to C itself and that, for any given RF phase jitter, it is maximum for the phase set at zero crossing.

1.7 RF Bunching

RF compression refers to two techniques of bunch-length shortening that exploit the relative longitudinal slippage of low-energy electrons as induced by a suitable arrangement of the RF linac phase. In RF 'ballistic bunching', an energy chirp is imparted to the beam in a cavity run off-crest. If the beam energy is low enough (particles are *not* in the *ultra*-relativistic limit yet), a difference in longitudinal momentum translates into a difference in longitudinal velocities, and therefore in arrival time at a given position downstream of the cavity. In order for a ~ 10 MeV

bunch to be shortened by, say, a factor ~ 5, a drift length of the order of ~ 1 m or longer may be needed after the cavity. Bunch shortening happens if the bunch head is at lower energies than the bunch tail. Most of bunch shortening happens outside the cavity, and the energy-position correlation established in the cavity tends to be removed later in the drift section. However, the final longitudinal phase space usually shows strong non-linearities as induced by both the RF curvature and space-charge forces, which are enhanced by the increased charge density.

RF 'velocity bunching' differs from ballistic bunching in that the phase-space rotation happens *inside* an RF linac, still run off-crest, and the energy chirp is smoothly removed in the linac itself through electrons' longitudinal slippage and acceleration. Similarly to the ballistic bunching, the minimum bunch length achievable with this technique is determined by the distortion of the final phase space induced by RF field nonlinearities and space-charge forces.

In order to follow the longitudinal particle motion in the presence of RF compression, we assume the beam to be accelerated in a series of RF standing wave structures. The evolution of the beam mean energy gain and the beam arrival time along the beam line is:

$$\begin{aligned} \frac{\mathrm{d}\gamma(s)}{\mathrm{d}s} &= \alpha[\cos(\phi)+\cos(\phi+2ks)], \\ \mathrm{d}t = \frac{\mathrm{d}s}{\beta c} &= \mathrm{d}s\frac{\gamma(s)}{c\sqrt{\gamma(s)^2-1}}, \end{aligned} \tag{26}$$

where we introduced the 'electron capture' parameter $\alpha \equiv \frac{eE_{z,0}}{2km_ec^2}$ and the RF phase φ; the factor '2' in α disappears for TW structures. By integration of the previous equations one eventually finds:

$$\begin{aligned} \gamma(s) &\cong 1+\alpha\left\{ks\cos\phi(s)-\frac{1}{2}\left[\sin(\phi)-\sin(\phi+2ks)\right]\right\}, \\ \phi(s) &\cong \phi_0-\frac{1}{2\alpha\cos\phi_0}\left[\sqrt{\gamma^2-1}-(\gamma-1)\right]_{(s\approx 0)} \rightarrow \phi_\infty = \phi_0-\frac{1}{2\alpha\cos\phi_0} \end{aligned} \tag{27}$$

The asymptotic value of the beam phase is for $\gamma >> 1$. Figure 3 shows particle trajectories in the longitudinal phase space. In that example, acceleration is maximum for $\varphi = \pi/2$.

A rough estimation of the bunch length compression factor in the limit of high beam energy can be obtained by recalling that bunch-length shortening means also compression of an incoming time or phase jitter (see Section 5). We differentiate the phase expression in Eq. 27 and find:

$$C \approx \frac{\mathrm{d}\phi_0}{\mathrm{d}\phi_\infty} = \left[1-\frac{\sin\phi_0}{2\alpha\cos^2\phi_0}\right]^{-1} \tag{28}$$

For example, for $\alpha = 2$ and $\varphi_0 = \pi/3$, $C \approx 10$.

Although neglected so far, the longitudinal particle dynamics at beam energies as low as considered in this section is intrinsically coupled to the transverse one by means of the repulsive 3D space-charge forces. In practical situations, the compression factor achieved through RF compression is limited by the tolerable transverse emittance dilution induced by space-charge forces. This effect can be mitigated by the application of external magnetic focusing, such as solenoidal fields, which counteract the particles' repulsion ('emittance compensation').

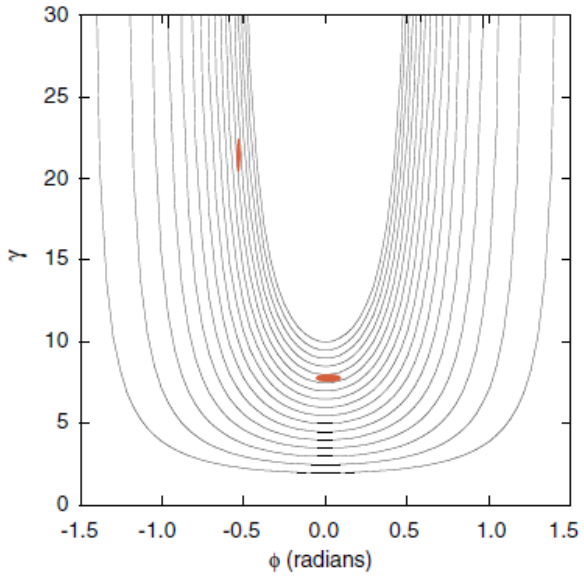

Figure 3: Phase-space apparent rotation in RF sinusoidal accelerating field, leading to bunch-length shortening for a bunch injected near the phase of zero crossing. Published in S.G. Anderson *et al.*, *Phys. Rev. ST Accel. Beams* **8** (2005) 014401. Copyright of American Physical Society.

2 Determination of the Compression Scheme for CompactLight

2.1 Choice of RF compression

RF bunching can be implemented either through ballistic bunching or velocity bunching. Below, we list the considerations leading to the choice of RF bunching.

1. Compactness and higher beam energy per unit length of the beam line suggests the adoption of velocity bunching vs. ballistic bunching.

2. For any given total compression factor, the shorter the bunch at the entrance of the magnetic compressor (BC1), the higher the linear energy chirp at the compressor for any given correlated energy spread, the lower the momentum compaction required in the compressor for a given final peak current, the weaker the effect of CSR on the beam emittance.

3. In the range of parameters of interest for CL, velocity bunching showed the capability of increasing the bunch peak current by a factor 3-6 while preserving the beam emittance at the same value of the uncompressed bunch. This is basically at the expense of 20-40 MeV lower beam energy at BC1, for the same injector length.

4. A shorter bunch from the injector samples less RF curvature in the following structures before reaching BC1, and is there expected to partially alleviate the constraint on the linearizer peak voltage, at any given RF frequency.

Because of these considerations, velocity bunching is recommended for the CL injector.

2.2 Choice of Injector RF frequency

By virtue of higher RF frequency, the accelerating field gradient of both Gun and accelerating structures is higher, therefore the beam line is expected to be shorter, for any given final beam energy. However, higher frequency is obtained at the expense of more difficult technological realization of RF components, typically lower reliability, higher geometric impedance as due to smaller transverse iris radius, and higher RF frequency of the harmonic cavity for linearization of the compression process (linearizer).

It is worth considering that, for any given compression factor in BC1 in the range 5-20, associated to $|R_{56}|$ in the range 10-50 mm, and for a beam energy at BC1 in the range 200-300 MeV:

- an S-band injector implies a peak voltage of 10-20 MV from an X-band linearizer (4^{th} harmonic)
- a C-band injector would require a 4 times higher peak voltage in the X-band (2^{nd} harmonic),
- or a 2.3 times lower peak voltage in the Ka-band (6^{th} harmonic);
- an X-band injector would require almost 2 times higher peak voltage in the Ka-band (3^{rd} harmonic).

One should also consider that, since the linearizer runs at the decelerating phase, the higher its peak voltage, the lower the beam energy at BC1 for any given space devoted to the injector; alternatively, the higher the peak voltage, the longer the injector will be for any given beam energy at BC1.

The physical longitudinal space required by the linearizer is $\sim$0.5 m for the X-band (for a peak gradient of 65 MV/m), and $\sim$0.1 m for the Ka-band (for a peak gradient of 100 MV/m). However, one should keep in mind the need of beam focusing inside the linarizer, whose iris radius can be extremely small. For the X-band and Ka-band case, respectively, we assume a = 3.5 mm and a = 1.3 mm. For a beam projected normalized emittance of 0.2 mm mrad (rms value), and in order to have an rms beam size at least 10 times smaller than the radius, we require a betatron function in both planes not larger than 50 m for the tighter case (Ka-band). This is definitely feasible with standard quadrupole magnets.

As a consequence of the considerations above, the most cost-effective and compact injector RF frequency in the presence of RF linearization is (the lengths below are referred to the space needed for reaching a beam energy of approximately 100 MeV):

i) S-band injector + X-band linearizer, for a total injector length of 20 m;

ii) C-band injector + Ka-band linearizer, for a total injector length of 8 m;

iii) X-band injector with a total injector length of less than 3 m.

Figures 4, 5, and 6 compare the particle tracking results of a full S-band, C-band, and X-band photo-injector, respectively, optimized with and without velocity bunching. The laser longitudinal duration was optimized according to the minimum emittance requirement. The velocity bunching option provides beam brightness $\sim$3 to $\sim$8 times higher than without RF compression. Figure 7 shows the required peak voltage at the linearizer, for the options i) and ii) listed above.

A choice among the three options i), ii), iii) for the CL injector should be based, for same target performance of the systems, by taking into consideration the technical feasibility and technoilogical risks associated to the different RF options.

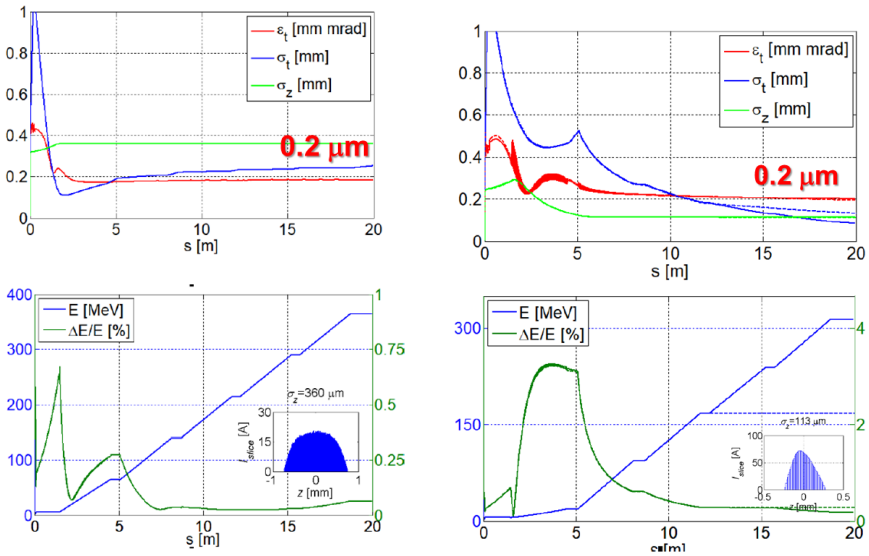

Figure 4: Beam dynamics of a 75 pC bunch charge from Cu Cathode in a full S-band photo-injector, with (right) and without (left) velocity bunching. Velocity bunching allows the increase of the peak current by a factor 3 while preserving the transverse emittance. The peak electric field at the cathode is 120 MV/m. TStep particle tracking run.

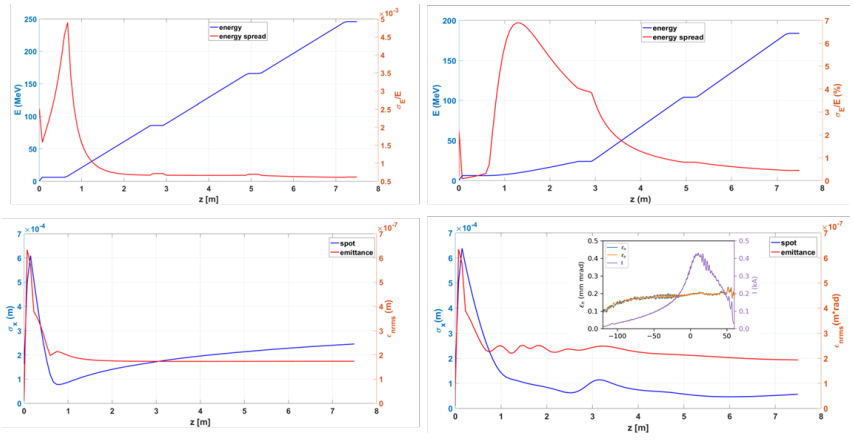

Figure 5: Beam dynamics of a 100 pC bunch charge from Cu Cathode in a full C-band photo-injector, with (right) and without (left) velocity bunching. Velocity bunching allows the increase of the peak current up to a factor 8 while preserving the transverse emittance. The peak electric field at the cathode is 240 MV/m. TStep particle tracking run.

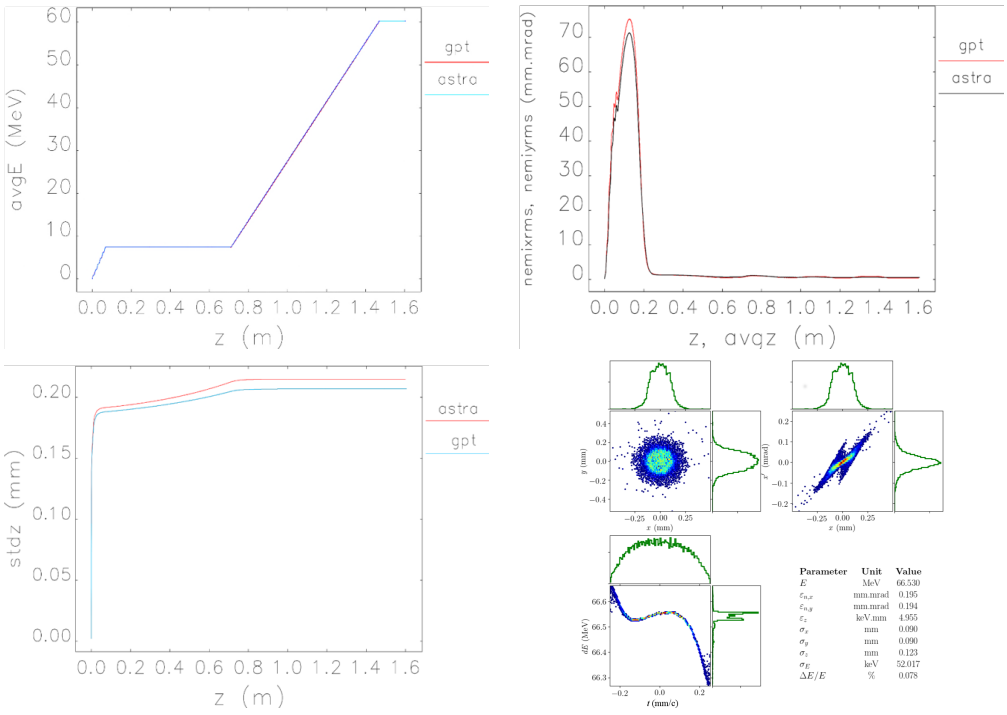

Figure 6: Beam dynamics of a 100 pC bunch charge from the Cathode in a full X-band photo-injector, without velocity bunching. The peak electric field at the cathode is 250 MV/m. The top-left plot shows the energy profile, the top-right plot the transverse emittance, and the left-bottom plot the bunch length along the injector. At the bottom-right, the phase space plots at the injector exit, with a table with the main bunch parameters. ASTRA and GPT particle tracking run.

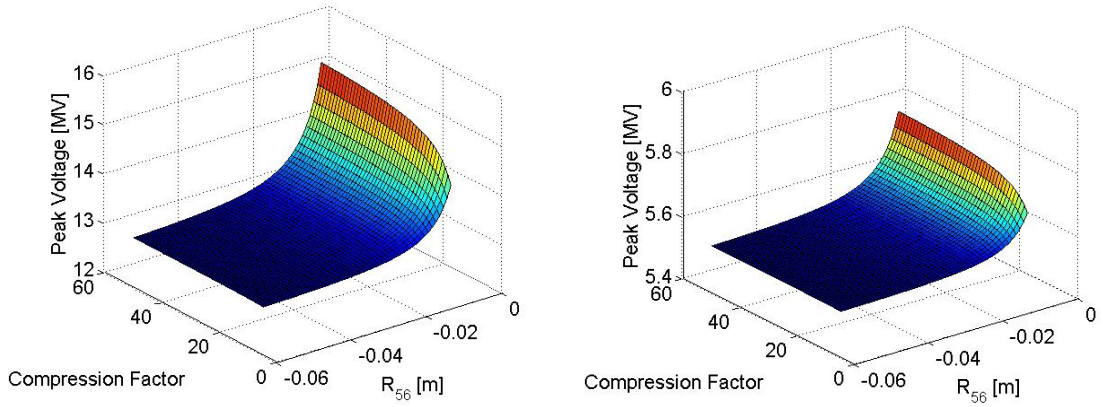

Figure 7: Peak voltage of the linearizer as a function of momentum compaction and compression factor in the magnetic chicane (see text for parameters), for the S-band linac + X-band linearizer (left) and C-band linac + Ka-band linearizer (right).

2.3 Choice of magnetic compressor geometry

Magnetic insertions suitable to bunch compression include 4-dipole chicane, dog-leg, and arc. The R_{56} of a chicane has negative sign (in the absence of strong quadrupole magnets), and this implies a linear positive energy chirp at the entrance of the compressor, i.e., the bunch head has a lower energy than the tail. With this configuration, the longitudinal geometric wakefields in the linac induce an energy chirp of opposite sign; the effect is stronger for shorter bunches, at any given bunch charge. The effect can be used to cancel the energy chirp required by compression in the chicanes. However, simulation studies show that the wakefield tends to over-compensate the initial positive chirp for a linac length which is required to reach beam energy of 4 GeV or higher. A minimization of the energy chirp at the linac end would require a large positive initial chirp, thus large off-crest acceleration in the injector area. A projected rms relative energy spread of the order of 0.5% is expected at BC1.

It is worth noticing that, for bunch chares in the 50 - 100 pC range and final peak current higher than $\sim$3 kA, off-crest acceleration of the last part of the linac is not able to fully cancel the residual negative chirp in any practical way. A projected rms energy spread of approximately at the level of 0.01% is expected at the linac end, at beam energies in the range 6-8 GeV, and final peak current in the range 3-8 kA.

Dog-legs and arcs provide positive R_{56}, therefore they require a negative energy chirp at their entrance. In this case, the chirp required by the magnetic compression would sum up to the chirp imparted to the beam by the linac wakefields, and the compensation of the final energy spread would turn out to be even worse than in the case of the chicanes. Alternatively, one could think of profiting of the wake-induced negative chirp in front of the magnetic insertion, thus maximizing the acceleration efficiency in the injector area, but still at the expense of the final energy spread. One should also notice that dog-legs and arcs change the beam direction of propagation, and have therefore consequences on the infrastructure footprint and volume of the buildings.

Chicanes are not very suitable for magnetic linearization through, for example, sextupole magnets. The reason is that sextupoles would require π-betatron phase advance between them in order to cancel geometric and chromatic aberrations. This in turn implies quadrupoles in the chicane, and a total length of the magnetic insertion at least twice longer than for a simple 4-dipole chicane. On the contrary, dog-legs and arcs contain quadrupole magnets in their native configuration, and space for sextupole magnets. The total length of a dog-leg, however, would turn out to be approximately twice longer than for a 4-dipole chicane.

In summary, the adoption of chicanes in combination with RF linearization provides the most compact solution for the compression scheme, and is expected to provide similar performance in the preservation of the beam brightness w.r.t. other solutions. It is worth noticing, however, that the beam longitudinal phase expected for a full X-band injector has a negative linear energy chirp which facilitates compression with a dog-leg or arc-like geometry of the compressor. The convenience of either one or the other option should be evaluated on the basis of the minimization of costs of the building volumes.

Magnetic chicanes with RF linearization is therefore considered the nominal compression scheme for CL for an S-band or C-band-based injectors. Either dog-leg or arc geometry could be considered for a full X-band injector.

3 CompactLight FEL Working Point

3.1 Electron Beam Parameters

The preliminary definition of a working point for the SX and HX e-beam delivery system is necessary in order to asset a preliminary compression scheme, thus a preliminary design of magnetic compressors and definition of the compression factors. Bunch length compression defines in turn, for example, the amount of uncorrelated energy spread at the undulator, indicates if a laser heater may be required or not, sets the maximum peak current and minimum bunch duration as a function of the tolerable residual energy chirp and projected emittance, *etc*. For this reason, tentative e-beam parameters as well as tolerance for slice and projected parameters are discussed below as a prologue to a more detailed description of the compression scheme and of its performance.

We anticipate that semi-analytical estimations of the electron beam parameters at the undulator for the soft (SX) and hard X-ray (HX) FEL line suggest a bunch charge in the 20-100 pC range, final bunch durations FWHM in the range 1-50 fs, and final beam energy up to 7 GeV. We will consideri tentative values of 4 GeV for the SX and 7 GeV for the HX. The shortest wavelength of interest for the SX and the HX FEL is, respectively, 0.6 nm (2.0 keV) and 0.08 nm (16 keV).

In order to start defining a realistic magnetic compression scheme, we will tentatively rely on the following choices and assumptions:

- same electron beam parameters for both SX and HX FEL, with the exception of the final beam energy and final energy spread. Since we assume same injector bunch, this implies same compression scheme for both FEL lines, whose simultaneous operation at 100 Hz is a second level priority of the CL project;

- a maximum 100-fold two-stage compression scheme based on chicanes is assumed. Multiple stages as well as different compressor geometries could be considered in a successive iteration;

- the current profile from the injector is fitted with a square profile, so that the peak current is defined in terms of the rms bunch durations as $I = Q/(\sqrt{12}\sigma_t)$;

- slice rms normalized beam emittance at the exit of the injector follows the empirical rule $\varepsilon_n[\mu m\, rad] \approx \sqrt{Q[nC]}$, which fits most of the state-of-the-art S-band SLAC-type injector performance

The e-beam parameters at the exit of the injector are defined as follows, and summarized in Table 1.

1. The diffraction limit condition for the normalized emittance at the minimum wavelength of interest for SX and HX, gives 0.4 and 0.08 mm mrad. Since semi-analytical estimations of FEL performance are compatible with a higher beam emittance for the HX, and referring to preliminary injector simulations, we choose an intermediate value of 0.2 mm mrad. This is intended to be the slice emittance at the undulator, and basically the projected value at least in the low energy part of the main linac. While some projected emittance degradation might be foreseen from the injector to the FEL, we assume that the slice one is preserved. Thus, full transverse coherence is ensured at 7 GeV down to 0.18 nm (7 keV).

2. The aforementioned rule-of-thumb for the emittance as a function of the bunch charge suggests Q $\approx$ 75 pC.

3. We assume final bunch duration of 2 fs rms or 7 fs fwhm. We also consider a "compression efficiency" of 0.9, which takes into account the non-uniformity of the current profile after magnetic compression. Thus, the final peak current (to be intended in the bunch core) is expected at the level of 6 kA. For a maximum compression factor C=100, the initial peak current shall be 60 A. This corresponds to the initial rms bunch duration of approximately 0.25 ps. Such a short-high current bunch at the exit of the injector is assumed to be produced with velocity bunching.

4. The initial rms uncorrelated energy spread is assumed to be 2 keV. A compression factor C=100 implies a minimum slice energy spread at the undulator of 200 keV. Residual energy chirp and, most importantly, the adoption of a laser heater for suppression of microbunching may justify a final value as high as 1 MeV (note: this estimation matches the LCLS operational parameters for a comparable C, at the bunch charge of 250 pC). Thus, the relative slice energy spread at the beam energy of 4 and 7 GeV is, respectively, 2.5×10^{-4} and 1.4×10^{-4}. Semi-analytical estimations suggest that this value can be relaxed up to a factor 3 or so, at the expense of some degraded FEL performance. It is worth noticing that, assuming a two-stage magnetic compression by a factor 100 or so, the final slice energy spread of 1 MeV implies beam heating at 10 keV before compression (all rms values).

5. The upper limit for the correlated energy spread, i.e. the linear energy chirp at the undulator, is $\sigma_{\delta,sl} = \sqrt{(\sigma_{\delta,u})^2 + (\frac{hN_u\lambda}{\sqrt{2\pi}})^2}$, where h is the energy chirp and $N_u\lambda$ the radiation slippage in the undulator. We impose $\sigma_{\delta,sl} = 1.6\rho_{FEL} \approx 0.06\%and0.03\%$ for the SX and HX respectively. For an rms uncorrelated energy spread of 1 MeV, final rms bunch duration of 2 fs, undulator period of 1.6 cm and 30 m total undulator length, we obtain $\sigma\delta, cor \approx H\sigma_z \leq 0.07\% and \leq 0.2\%$. The stronger constraint on the chirp control is for the SX line, due to the longer slippage length and the lower beam mean energy. Any residual energy chirp required for bunch compression and chirp induced by longitudinal wakefields (of opposite sign of the previous one, and expected to be the dominant source of residual chirp at the undulator) shall therefore be compensated with a proper linac RF phasing.

3.2 Compressor Parameters vs. Bunch Length

We model the bunch length compression starting from the longitudinal coordinate inside the bunch of a generic particle, at a distance z from the centroid (z=0), up to second order in the particle coordinates:

$$z_f = (1+R_{56}h_i)z_i + T_{566}h_i^2 z_i^2 + R_{56}\delta_{u,i} + T_{566}h_i z_i \delta_{u,i} + T_{566}\delta_{u,i}^2 \approx R_{56}\delta_{u,i} + (1+R_{56}h_i)z_i + T_{566}h_i^2 z_i^2 \quad (29)$$

where $\delta_{u,i}$ is the initial fractional uncorrelated energy spread, $h = \frac{1}{E_0}\frac{dE}{dz}$ is the linear energy chirp, E_0 is the beam mean energy (assumed constant through the compressor), R_{56} and T_{566} first and second order transport matrix terms, respectively, associated to first and second order momentum compaction, and the approximation on the r.h.s. of Eq. 29 is justified as long as

$T_{566}\delta_{u,i} \ll R_{56}$. We introduce $C = \frac{1}{|1+h_i R_{56}|}$ as the linear compression factor. Passing from Eq. 29 to the second-order momenta of the particles distribution, and considering that for a Gaussian $\left\langle z_i^4 \right\rangle = 3\left\langle z_i^2 \right\rangle^2$, we obtain:

$$\sigma_{z,f} = \sqrt{(\frac{\sigma_{z,i}}{C})^2 + (R_{56}\sigma_{\delta,i})^2 + (3T_{566}h_i^2\sigma_{z,i}^2)^2} \tag{30}$$

Eq. 30 allows us to estimate the maximum value of R_{56} vs. the specified bunch length at the exit of the chicane, in the assumption of pure linear motion and a maximum value for the initial uncorrelated energy spread of 10 keV (dominated by beam heating at maximum level). The mean energy at BC1 is assumed to be 300 MeV. Compressed bunch duration of 250 fs/100 = 2.5 fs therefore implies a *total* momentum compaction $|R_{56}|$ << 100 mm. The minimum correlated relative energy spread at the entrance of BC1 is $\sigma_{\delta,cor} \approx h_i\sigma_{z,i} \cong (1-\frac{1}{C})\frac{\sigma_{z,i}}{R_{56}} = 0.15\%$. A possible set-up of the compression in BC1 is $\sigma_{\delta,cor} \approx 0.4\%$ and $R_{56} \approx -18$ mm, for $C = 13$; the expected rms bunch duration is 20 fs. Repeating the same calculation for BC2 at the tentative energy of 2 GeV, where we assume an initial uncorrelated energy spread of 130 keV (10 keV from laser heater times 13-fold compression in BC1) and a specified final rms bunch duration of 2 fs, we estimate $\sigma_{\delta,cor} \approx 0.1\%$ and $R_{56} \approx -10$ mm; the expected rms bunch duration is 2.5 fs.

It is worth noticing that the proposed values for the correlated energy spread are one order of magnitude higher than the expected uncorrelated ones, which justifies the approximated expression for the linear energy chirp. Moreover, with the compression parameters proposed above, the second order term in the r.h.s. of Eq. 30 can be neglected both for BC1 and BC2.

The peak voltage of the RF high harmonic cavity for linearization of the magnetic compression is estimated with Eq. 9. For an S-band injector and a 4^{th} order higher harmonic, we require a peak voltage of 14 MV. A C-band injector and 6^{th} harmonic Ka-band linearizer we require a peak voltage of 6 MV.

Owing to the relatively short bunch duration along the whole delivery system, a given correlated energy spread is reached at the expense of larger off-crest phasing than for longer bunches (see Eq. 2. Linacs run far from the crest amplify the final beam energy jitter and bunch length jitter, for any given voltage and phase jitter budget (see Eq. 24 and 25. For example, the maximum distance of the linac RF phase from the accelerating crest which is compatible with a given compression factor and bunch length relative jitter can be calculated with Eq. 25, and is plotted in Fig. 8 for estimated values of the CL linac.

3.3 Compressor Parameters vs. Beam Emittance

As far as the electron beam is not approaching the point of full compression (this is defined by an upright longitudinal phase space for minimum bunch duration), we assume that slice emittances are unperturbed by the compression process. The projected horizontal emittance, instead, is affected by CSR chromatic kicks.

The maximum tolerable projected emittance at the undulator is estimated through the revised Tanaka's angle formalism, which is expected to provide a conservative estimation for the final emittance value. The FEL gain length degraded by correlations in the transverse beam phase space, projected over the whole bunch duration, is $L_G \approx \frac{L_{G,3D}}{1-2\pi\theta_{pr}^2/\theta_c^2}$, where $\varepsilon_{n,f} \approx \varepsilon_{n,i}\sqrt{1+\frac{\gamma\beta_u\theta_{pr}^2}{\varepsilon_{n,i}}}$ and $\theta_c = \sqrt{\lambda/L_{G,3D}}$. The nominal 3-D gain length is estimated to

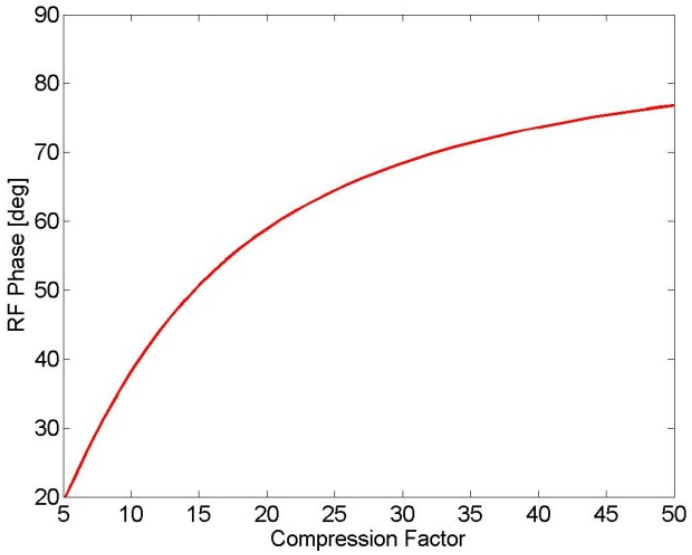

Figure 8: RF phase of injector linac vs. linear compression factor at the *first* chicane, for assumed value of 0.1 deg rms phase jitter and specified 1% rms bunch length jitter. The accelerating phase is at 90 deg. The compression scheme discussed above suggests a linac phase not exceeding 60 deg (30 deg from the crest).

be not longer than 2 m both for the SX and HX. We assume average betatron functions of 10 m in the undulator. An elongation of the gain length by not more than 10% implies an rms normalized projected emittance (in both planes) not larger than 0.4 and 0.3 mm mrad, for the SX and HX respectively. Such a growth is expected to be dominated by coherent synchrotron radiation (CSR) emission in magnetic compressors and by geometric transverse wakefields in the small iris X-band linac structures.

According to the theory of optics balance in the presence of CSR, we parametrize its final value as follows:

$$\varepsilon_{nx,f} = \sqrt{(\varepsilon_{nx,i})^2 + \varepsilon_{nx,i}\gamma H_x \sigma^2_{\delta,CSR}} \tag{31}$$

Here γ is the Lorenz factor for the beam mean energy, $H_x \equiv [\eta_x 2 + (\beta_x \eta'_x + \alpha_x \eta_x)2]/\beta_x$ is expressed in terms of Twiss parameters and energy dispersion functions at the location of dipole magnets, and $\sigma_{\delta,CSR}$ takes into account 1-D CSR dynamics through variation of the fractional longitudinal momentum along the bunch. Since $\sigma_{\delta,CSR}$ is inversely proportional to the bunch length, the transverse CSR effect in a four dipoles magnetic chicane is dominated by the radiation emission in the second half of the system, where the bunch reaches its shortest duration. We consider typical values in the compressor such as bending angle $\theta \leq 0.1$ rad, dipole length l $\approx$ 0.3 m, $\eta \leq 0.2$ m and $\beta \geq 1$ m. We assume a beam waist in the second half of the chicane and β that remains in the range 1-5 m across it. Then, $H \approx \eta^2/\beta \approx 0.01m$ at the end of the 3^{rd} dipole and $H \approx \beta \eta'^2 \approx \beta \theta^2 \approx 0.03m$ at the entrance of the $4^t h$ dipole. CSR contribution from the 3^{rd} dipole is actually suppressed with respect to the 4$^{\text{th}}$ because the beam reaches its final shortest length only at the very *end* of that magnet. Hence, $\sigma_{\delta,CSR}$ induced in the 3^{rd} dipole can be up to $\sim$C times smaller than in the 4$^{\text{th}}$ dipole, where C is the compression factor. In conclusion, Eq.3.3.1 prescribes to shrink the h-function at the entrance of the fourth

dipole in order to suppress CSR-induced emittance growth. When the bending angle is fixed and small ($\theta << 1$) and in the presence of a beam waist, this prescription involves shrinking β in proximity of the 4th dipole magnet. For those reasons, we estimate $\sigma_{\delta,CSR}$ as only due to the compressed bunch in the very last dipole. For a Gaussian line-charge distribution emitting in the CSR in steady-state approximation, it reads:

$$\sigma_{\delta,CSR} = 0.2459 r_e C^{4/3} \frac{N_e R^{1/3} \theta}{\gamma \sigma_{z,i}^{4/3}} \tag{32}$$

where r_e is the classical electron radius, N_e is the number of electrons per bunch, R and θ are the dipole's bending radius and angle respectively, and C is the linear compression factor through the compressor. In order to estimate the CSR-induced projected emittance growth in BC1 and in BC2, we have to define the geometry of the two chicanes. For the sake of compactness, we limit the length of both chicanes to 10 m; 1 m drift length in between the two inner dipoles is foreseen to install diagnostics. Some tentative parameters are listed in Table 2. The two chicanes are made of identical components, where BC2 is naturally exploiting a higher magnetic field, but still much lower than the typical value of iron saturation (around 1.2 T). With optics parameters inside the chicanes listed in Table 2, the order of magnitude of the CSR-induced relative energy spread is $\sigma_{\delta,CSR} \approx 5 \times 10^{-4}$ in BC1 and $\sigma_{\delta,CSR} \approx 10^{-4}$ in BC2. The projected emittance values at the exit of the compressors, also listed in Table 2, are estimated by considering the perturbation due to CSR only (linac transverse wakefield effect is neglected at this stage).

3.4 One-Dimensional Particle Tracking

The beam and machine parameters discussed above were plugged into the 1-D tracking code LiTrack for verification. The code includes the second order optics term in the chicanes and longitudinal geometric wake functions. These were generated according to Bane's model for an iris radius of 10 mm in the S-band linac upstream of BC1, and an average radius of 3.5 mm in the X-band structures. The initial charge distribution is assumed to be parabolic and with a linear chirp out from the injector of 0.5%, at the beam energy of 160 MeV. Figure 9 shows the tracking results along the delivery system after fine tuning of the input parameters in order to obtain a final rms bunch duration of 2 fs. The whole linac is assumed to run at 100 Hz; in this configuration, the SX and the HX FEL can run simultaneously, assuming that the electron beam is extracted from the main X-band linac at the intermediate energy of $\sim$3.6 GeV, immediately after compression in BC2.

Another independent 1D tracking code has been written for fast tracking and optimization as well, Track1D [5]. Similar to LiTrack, it simplifies the chicane to the second order and includes short-range longitudinal wake field by C. Bane's model. The X-band structure is assumed to have an average aperture of 3.5 mm while the K-band, which is used to linearise the energy chirp, is assumed to have an average 2 mm aperture, 0.75 m length and work with a gradient of 25 MV/m. Figure 10 shows the tracking results for the linac taking the distribution from the X-band injector shown in Fig. 6. In this configuration, the linac is assumed to run at 100 Hz and HX FEL is generated at 5.5 GeV.

Table 1: Initial and final (at the undulator) electron beam parameters estimated for the definition of the magnetic compression scheme, and tentative parameters for the soft (SX) and hard (HX) X-ray FEL.

Electron Beam	**Value**	**Unit**
Final Mean Energy	4.5 (SX) / 7 (HX)	GeV
Bunch Charge	75	pC
Initial Bunch Duration, RMS	250 (VB)	fs
Initial Peak Current	0.06	kA
Initial Uncorrelated Energy Spread, RMS	2	keV
Laser-Heater-Induced Uncorr. En. Spread, RMS	< 10	keV
Initial Normalized Slice Emittance, RMS (x,y)	0.2, 0.2	μ m rad
Initial Normalized Projected Emittance, RMS (x,y)	0.2, 0.2	μ m rad
Final Bunch Duration, RMS	≈ 2	fs
Final Peak Current	≈ 5	kA
Final Total Energy Spread, RMS	< 2 (SX) / < 8 (HX)	MeV
Final Relative Slice Energy Spread, RMS	< 0.03 (SX) / < 0.03 (HX)	%
Final Normalized Slice Emittance, RMS (x,y)	0.2, 0.2	μm rad
Final Normalized Projected Emittance, RMS (x,y)	< 0.4, < 0.3	μm rad
Free Electron Laser		
Minimum FEL Fundamental Wavelength	0.6 (SX) / 0.08 (HX)	nm
FEL Parameter	0.05 (SX) / 0.02 (HX)	%
Undulator Period Length	1.5	cm
Total Undulator Length (excluding drifts)	20 (SX) / 30 (HX)	m
Number of Undulator Periods, Total	3000 (SX) / 4500 (HX)	
FEL Slippage Length at minimum wavelength	8 (SX) / 0.7 (HX)	fs
Average Betatron Function in Undulator	10	m

Table 2: Parameters of magnetic compressors and linac (out of injector). An S-band injector and X-band linearizer is assumed.

Magnetic Compressors		
Compression Factor, BC1 x BC2	13×8	
Mean Energy at BC1	0.294	GeV
Correlated Relative Energy Spread at BC1, RMS	0.45	%
R_{56} of BC1	-17.5	mm
BC1 Bending Angle	70	mrad
BC1 Dipole Field	0.2	T
BC1 Outer Drift Lengths	2.5	m
BC1 Total Length	8	m
BC1 CSR-Induced Relative Energy Spread, RMS	0.05	%
Horiz. Betatron Function in the BC1 fourth magnet	0.5	m
Horiz. H-function in the BC1 fourth magnet	20	mm
Horiz. Normalized Projected Emittance at BC1 Exit, RMS	0.27	μm rad
Mean Energy at BC2	2.65	GeV
Correlated Relative Energy Spread at BC2, RMS	0.07	%
R_{56} of BC2	-10.0	mm
BC2 Bending Angle	40	mrad
BC2 Dipole Field	0.6	T
BC2 Outer Drift Lengths	2.5	m
BC2 Total Length	8	m
BC2 CSR-Induced Relative Energy Spread, RMS	0.01	%
Horiz. Betatron Function in the BC2 fourth magnet	0.5	m
Horiz. H-function in the BC2 fourth magnet	3	mm
Horiz. Normalized Projected Emittance at BC2 Exit, RMS	0.30	μm rad
Linac		
S-band Linac Energy Range	0.16 - 0.30	GeV
S-band Linac Length	7	m
S-band Accelerating Gradient	25	MV/m
S-band Linac RF Phase	-30	deg
X-band Linearizer Peak Voltage	14	MV
X-band Linearizer RF Phase	200	deg
X-band Linac Energy Range	0.30 - 7.0	GeV
X-band Linac Length	120	m
X-band Accelerating Gradient	65	MV/m
X-band Linac RF Phase	-30 / 0	deg

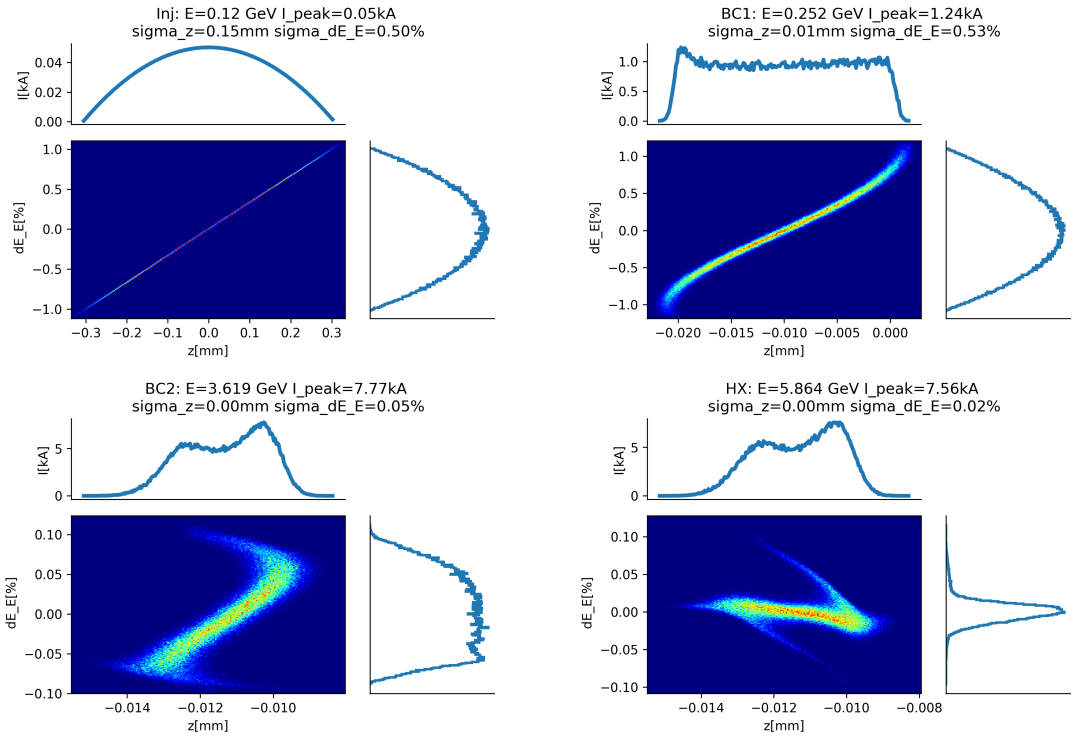

Figure 9: From top left to bottom left, the subplots refer to: after laser heater, exit of BC1, exit of BC2, SX extraction point, HX extraction point. In each subplot: current intensity profile, phase space distribution and relative energy spread profile.

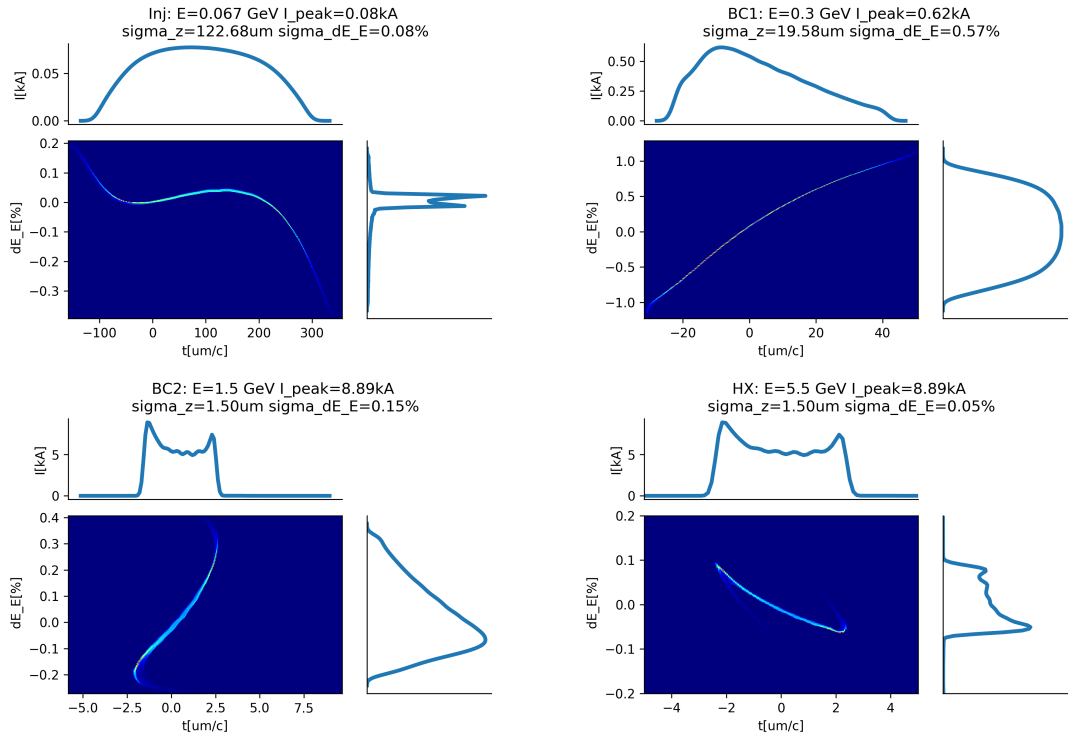

Figure 10: Phase space distributions for a full X-band solution. Two chicanes are located at 300 Mev and 1.5 GeV, respectively. From top left to bottom left, the subplots refer to: exit of injector, exit of BC1, exit of BC2, HX extraction point. In each subplot: current intensity profile, phase space distribution and relative energy spread profile.

3.5 Sensitivity and tolerance study

We also need to address the sensitivity for the scheme that we adopted to compress the beam. Table 4 shows the sensitivity of the beam parameter at the linac end for each component of the linac which we designed for the full X-band solution (Fig. 10). The design values for each component are listed in Table 3. As expected, components before the two bunch compressors will greatly affect the arrival time and peak current at the linac end while the final energy mainly affected by the last section of linac (X2). It is worthwhile to point out that the 'peak current' change may not be so useful because due to wake field effects, the current intensity profile has two peaks at the bunch head and tail and they are very sensitive to these parameters as shown here.

Sensitivity studies can be used also to determine the tolerance for each component. Suppose that the FEL performance requires that beam parameters must be controlled within a range, this in return determines the tolerance acceptable for each component. For example, for the full X-band design, Table 5 shows the tolerance for each linac component to ensure that the arrival time change is less than 20 fs, peak current intensity change is less than 5% and final beam energy is within 0.05% change.

Table 3: Linac design parameters for full X-band solution.

RF structures		units	Bunch compressors		units
X0_voltage	257	MV	BC1_R56	-0.018	m
X0_phase	15	deg	BC1_T566	0.027	m
K_voltage	15	MV	BC2_R56	-0.012	m
K_phase	-180	deg	BC2_T566	0.018	m
X1_voltage	1.25	GV			
X1_phase	17	deg			
X2_voltage	4.14	GV			
X2_phase	15	deg			

Table 4: Sensitivity study for the full X-band linac design (layout: inj-X0-K-BC1-X1-BC2-X2) with two magnetic chicanes (Note that the amount of change can be positive or negative, the worst case is shown here)

Jittering source	amount	Arrival time [fs]	Peak current [%]	Energy [%]
Charge	1 pC	4.315	26.273	0.003
arrival time for injector	1 fs	0.144	1.803	0
X0 voltage	1%	225.551	231.032	0.521
X0 phase	1 deg	105.636	38.531	0.222
K voltage	1%	12.037	6.721	0.030
K phase	1 deg	0.615	11.847	0.005
X1 voltage	15.00	324.263	9.866	0.266
X1 phase	1 deg	176.307	153.672	0.130
X2 voltage	1%	0	0	0.729
X2 phase	1 deg	0	0	0.352

Table 5: Tolerance study for the full X-band linac design with two magnetic chicanes

jitter source	unit	Arrival time ≤ 20 fs	Peak current ≤ 5 %	Energy ≤ 0.05 %
Charge	%	4.35	0.304	8.10
injector arrival time	fs	135	18	430
X0 voltage	%	0.099	0.045	0.098
X0 phase	deg	0.2040	0.0848	0.2280
K voltage	%	1.64	0.89	1.62
K phase	deg	9.70	0.246	11.55
X1 voltage	%	0.062	0.580	0.196
X1 phase	deg	0.116	0.168	0.388
X2 voltage	%	-	-	0.068
X2 phase	deg	-	-	0.144

3.6 Coherent Synchrotron Radiation

Coherent Synchrotron Radiation (CSR) effects on the quality of ultra-relativistic beams have been addressed since the middle of 80's [6], i.e. since the advent of sub-picosecond long electron bunches as drivers of linac-based x-ray free electron lasers. The theoretical aspects are covered by a wide literature mainly focused on the transverse CSR induced phase space

emittance dilution when very short electron beams are bent in dipole magnet chicanes acting as bunch length compressors, or in beam delivery transfer lines and in turnaround arcs as well. Following the treatment reported in [7] the CSR effect can be seen as a cooperative radiation field generated at the tail of the bunch that can overtake the bunch head when the particles move on a curved trajectory, namely a similar but opposite phenomenon of the well-known wake-fields in accelerators generated by collective effects that act from the head to the tail of the electron bunches. An ultra-relativistic electron bunch in a magnetic field radiates coherently in the frequency range of $\omega \ll c/\ell_b$, with ℓ_b the bunch length and c the speed of light, namely this is also the tail of the single particle synchrotron radiation spectrum. The characteristic wavelength of the radiation is $\lambda_{cr} \sim R/\gamma^3$, where R is the orbit curvature and γ the relativistic factor and it is assumed that the bunch length is much larger than the incoherent radiation wavelength, i.e. $\ell_b \gg \lambda_{cr}$. The total intensity of the radiation spectrum generated by N electrons is the sum of the incoherent and coherent contributions:

$$\left(\frac{dI}{d\omega}\right)_{tot} = Ne\left(N_e + 1\right)\left|F\left(\omega\right)\right|\left(\frac{dI}{d\omega}\right)_e \tag{33}$$

where $F(\omega)$ is the Fourier transform of the longitudinal particle distribution; the coherent emission is N-times brighter than the incoherent one (typically $\sim 10^9$ higher), so representing a particularly severe collective effect. For the spectral coherent radiation intensity at low frequencies due to a bunch with Ne charge we have:

$$\frac{dI}{d\omega} \sim \gamma \frac{(Ne)^2}{R}\left(\frac{\omega\lambda_{cr}}{c}\right)^{1/3} \tag{34}$$

and the energy loss per unit length can be estimated as:

$$\frac{dE_{coh}}{cdt} \sim \int_0^{c/\ell_b} \frac{dI}{d\omega}\frac{d\omega}{c} \sim \frac{(Ne)^2}{\left(R\ell_b^2\right)^{2/3}} \tag{35}$$

Practically absent for smooth charge distribution and for frequencies $\omega \gg \dfrac{c}{\ell_b}$, while the region of frequencies $\omega \simeq c/\ell_b$ is the interesting one; here the radiation is a cooperative effect in parts of the bunch, but depends also on the charge distribution profile along the bunch and the same holds for the energy losses distribution. It is the CSR emission from trailing electrons and the absorption by the leading ones that causes a variation of the energy of the electrons along the bunch, i.e. a longitudinally correlated energy spread that occurs in a dispersive region and start betatron oscillations of different parts of the electron bunch (slices) around different dispersive orbits, resulting in an increase of the projected beam size and angular divergence (emittance) in the bending plane. More in detail in the case of an electron bunch with arbitrary distribution of the linear charge density $\lambda(s)$ that satisfies the condition:

$$\frac{R}{\gamma^3}\frac{d\lambda\left(s\right)}{ds} \ll \lambda\left(s\right) \tag{36}$$

i.e. with the characteristics bunch length much larger than R/γ^3 as mentioned before, the rate of the energy change of a leading electron under the action of the radiative force from an electron behind can be written as:

$$\left(\frac{dE}{d(ct)}\right)_{CSR} = -\frac{2e^2}{3^{1/3}R^{2/3}}\int_{-\infty}^{s}\frac{ds'}{(s-s')^2}\frac{d\lambda(s')}{ds'} \tag{37}$$

where the arc length s specifies the locations of the electron and for a Gaussian distribution:

$$\lambda(s) = \frac{N}{(2\pi)^{1/2}\sigma}\exp\left[-\frac{s^2}{2\sigma^2}\right] \tag{38}$$

it can be obtained:

$$\left(\frac{dE}{d(ct)}\right)_{CSR} \simeq -\frac{2Ne^2}{(2\pi)^{1/2}3^{1/3}R^{2/3}\sigma^{4/3}}F\left(\frac{s}{\sigma}\right) \tag{39}$$

where:

$$F(\xi) = \int_{-\infty}^{\xi}\frac{d\xi'}{(\xi-\xi')^{1/3}}\frac{de^{\xi'^{1/2}}}{dx'} \tag{40}$$

and σ is the rms bunch length.
The total CSR power can then be written as:

$$P_{CSR} = -\int_{-\infty}^{\infty}ds\lambda(s)\left(\frac{d\varepsilon}{d(ct)}\right)_{CSR} \tag{41}$$

and for the gaussian distribution case it becomes:

$$P_{CSR} \simeq \frac{3^{1/6}N^2e^2c}{2\pi R^{2/3}\sigma^{4/3}} \times \left[\Gamma\left(\frac{2}{3}\right)\right]^2. \tag{42}$$

The total CSR power for a bunch of electrons can also be expressed [8] in terms of the CSR wakefield $\tilde{W}(s)$ as:

$$P_{csr} = \beta ce\int_{-\infty}^{\infty}ds\tilde{W}_{CSR}(s)\lambda(s) \tag{43}$$

therefore with:

$$\tilde{W}_{CSR}(s) = -\sqrt{\frac{2}{\pi}} \times \frac{Ne}{\left(3R^2\sigma\right)^{1/3}}\int_{-\infty}^{s}\frac{ds'}{(s-s)}, \frac{d\lambda(s)}{3ds'} \tag{44}$$

It can be seen then that a coherent energy spread is generated within a bending system that may couple to the transverse (bending) plane coordinates through the chromatic transfer functions of the particular beamline even in the case of an achromatic one [9] an electron in fact that loses an amount of energy $\delta(s)\Delta E(s)/E_0$ at location s within the bending system will be transported to its end through the chromatic transfer functions, $\partial x/\partial\delta \equiv R_{16}(s)$ and $\partial x'/\partial\delta \equiv R_{26}(s)$, which map an off nergy particle from the point of energy loss into transverse phase space at the end of the bending system. The energy loss can be different for different particles and the resulting energy spread can dilute the transverse emittance in the bending plane depending on the coherence of the process, since a random process can result on an intrinsic emittance dilution that cannot be recovered while a coherent energy spread generates

a projected emittance dilution where correlations among the beam coordinates remain, and it can be seen as a reversible process. Expressing the phase space coordinates in the bend plane as the vector $\mathbf{x} = \begin{bmatrix} x & x' \end{bmatrix}^T$ the rms emittance ε is taken from the covariance of the particle ensemble:

$$\varepsilon^2 = \det\langle \mathbf{x} \cdot \mathbf{x}^T \rangle \tag{45}$$

If a particle loses or gain energy at a location s within a bending system, even achromatic, its final phase space coordinates at the end of the system will be altered with respect the on-energy particle as:

$$\mathbf{x}_s = \mathbf{x}_0 + \Delta\mathbf{x}(s) = \mathbf{x}_0 + \begin{bmatrix} R_{16}(s) \\ R_{26}(s) \end{bmatrix} \delta(s) \tag{46}$$

assuming:

$$\langle \mathbf{x} \rangle = \langle \Delta\mathbf{x} \rangle = 0 = \langle \delta \rangle. \tag{47}$$

Given an input emittance ε_0 the final emittance at the system end is:

$$\varepsilon^2 = \varepsilon_0^2 + \varepsilon_0 \left[\beta \langle \Delta x'^2 \rangle + 2\alpha \langle \Delta x \Delta x' \rangle + \gamma\beta \langle \Delta x^2 \rangle \right] + \langle \Delta x^2 \rangle \langle \Delta x'^2 \rangle - \langle \Delta x \Delta x' \rangle^2 \tag{48}$$

where β, α, γ are the nominal Twiss parameters at bending system end.

For the incoherent energy loss process the variance of Δx due to the incremental energy spread generated along s is:

$$\left\langle \Delta x^2 \right\rangle_{inc} = \int R_{16}(s)^2 \frac{d}{ds} \sigma_\delta^2 ds \tag{49}$$

while for the coherence process we have:

$$\left\langle \Delta x^2 \right\rangle_{coh} = \left(\int R_{16}(s) \frac{d\sigma_\delta}{ds} ds \right)^2 \tag{50}$$

From which it can be seen that the incoherence process is a summation of signed quantities which may vanish. The full emittance dilution for the coherent process is then [9]:

$$\varepsilon^2 = \varepsilon_0^2 + \varepsilon_0 \frac{1}{\beta} \left[\langle \Delta x^2 \rangle + \left(\alpha \left\langle \Delta x^2 \right\rangle^{1/2} + \beta \left\langle \Delta x'^2 \right\rangle^{1/2} \right)^2 \right]. \tag{51}$$

It is worth to notice that here a full coherence is assumed and a particle energy deviation is only function of its position along the bunch and this is a scalar equal for all particles at any particular location s along the beamline, but may vary with s for example due to the variation of the bunch length. Considering as an example the case of a periodic cell-arc with $(2n+1)\pi$ total phase advance, from the above discussion, the incremental rms coherent energy spread generated as “steady-state” CSR (i.e. without considering the transient region of the magnet fringe field) at each dipole slice in which we subdivide the magnet length, can be written as:

$$\Delta\sigma_\delta(s) \approx 0.22 \frac{r_e N \Delta L_B}{\gamma R^{2/3} \sigma_z^{4/3}} \tag{52}$$

that is basically what we have obtained so far, ignoring the vacuum chamber shielding, and where r_e is the classical electron radius, N is the bunch population, ΔL_B is the dipole magnet slice length, γ is the Lorentz energy factor, R is the bend radius and σ_z is the bunch length. For a constant bunch length, the net arc emittance growth is zero, but it oscillates with the periodicity of the arc, while compressing the bunch destroys the symmetry and produces a net growth of the emittance.

3.7 Options for minimization of CSR effects

The first obvious countermeasure against the emittance dilution is obtained with a sign reversal of equal contributions to the emittance dilution, i.e. with a half integer phase advance between two identical periods which have isochronous transportation between them [10], the basic requirements can be summarized as:

- a) there be transverse symmetry: the betatron and dispersion functions at “homologous” lattice points should be identical
- b) there be an appropriate phase relationship: the betatron phase advance between homologous lattice points should be a half integer
- c) the transport between homologous points should be such that the bunch length is the same, and each electron is at the same position within the bunch, at both points. This can be achieved through use of isochronous individual periods and isochronous transport from period to period.

On the same basis the combination of two compressor chicanes can help whenever the bunch length is instead supposed to vary and what mentioned at point c) is no more applicable [9]. In fact, in this case a double chicane can be designed of twice the length with separating optics (4 quadrupoles) to introduce a $-\mathbf{I}_{2\times 2}$ bend plane transfer matrix between chicane centers. The first chicane bend angles are reduced (increasing the bunch length there which reduces the CSR energy spread and the second chicane can be set to complete the final bunch compression such that dilution effects of the first chicane cancel with the second. The chicanes may also be empirically adjusted, if necessary, to minimize the observed dilution while maintaining final compression. Nevertheless, looking at eqs. 51 and 52 a good practice in designing a compressor chicane is to reduce to the minimum required the bunch charge and the Twiss betatron function on the bend plane at the end of the chicane where the bunch length is shorter. An intense study has been carried on the cancellation of the CSR induced emittance dilution by means of a more generic optics balance [11] in case of Double Bend Achromat lines, such as the ones required to transport the electron beam, or more generic Arcs with and without compression such as the ones designed for the Energy Recovered Linacs. In their works [12] they reviewed the Douglas idea using the C-S formalism and applying it to a dog-leg-like achromatic beamline (FERMI spreader), under the assumption that the bunch length and the longitudinal charge distribution of the bunch were not significantly changed by the beamline ($\mid R_{56} \mid \ll \sigma_z$) that implies the same energy kick in all dipoles and in presence of a relatively small σ_δ that allows to neglect the chromatic aberrations. The considered beamline is made of two identical double bend achromats as reported in the figure below. The same argument has been successfully applied even in case of non-symmetric lattices and also in case of longitudinal compression of the beam [13].

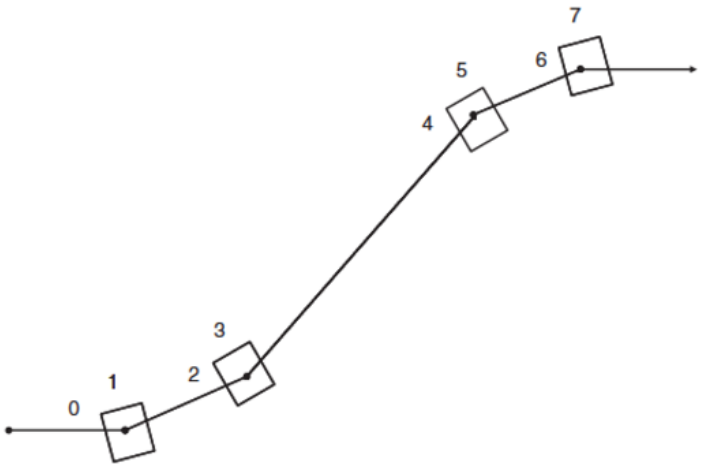

Figure 11: The FERMI Spreader (not to scale). The design optics gives a betatron phase advance of π in the bending plane between two consecutive dipoles. The quadrupoles present between the dipoles are not shown here.

Other methods look at the shaping of the longitudinal charge distribution in order to vanish the CSR induced energy spread [14], in fact starting from eq. 51 the more generic longitudinal steady state 1D CSR wakefield generated by the bunch in a bend can be written as:

$$W_{CSR}(s) = \int_{-\infty}^{s} ds' k_{csr}(s-s')\,\lambda(s') \tag{53}$$

where $k_{CSR}(s-s') = \left(\frac{dE}{d(ct)}\right)_{CSR}$. The resulting rms spread within the bunch in the CSR-induced energy change per unit length is given by:

$$\sigma_w = \sqrt{\left\langle W^2 \right\rangle_{\|} - \langle W \rangle_{\|}^2} \tag{54}$$

where for a given function ϕ it is denoted:

$$\langle \phi \rangle_{\|} = \frac{1}{N} \int_{-\infty}^{\infty} \phi(z)\,\lambda(z)\,dz \tag{55}$$

As already described, in presence of dispersion this variation of the wakefield-induced energy change along the bunch results in a growth of the projected emittance in the bend plane that can be expressed in terms of induced energy spread σ_E as:

$$\varepsilon \approx \sqrt{\varepsilon_0^2 + \varepsilon_0 \beta \left(\theta \sigma_E |E|\right)^2} \tag{56}$$

where β is the Twiss function at the bend exit, θ is the bending angle and E is the beam energy. The optimization goal is to find a density $\lambda(z)$ that minimizes eq. 55 for a fixed number of particle N and bunch length L. A general solution to the problem is constructed with a longitudinal wakefield of the form:

$$W(z) = -W_0 \text{ for} \in [a,b] \text{ and } L = b-a \tag{57}$$

for a longitudinal density $\lambda(z) = 0$ outside the interval $[a,b]$and that satisfies eq. 57 for all $z \in [a,b]$, the wakefield is uniform all over the bunch length and from eq. 54 is clearly $\sigma_W = 0$.

Therefore, the CSR induced growth of the emittance is eliminated from eq. 25 and a uniform energy loss remains along the bunch. Beyond this simple case, the authors solved the problem to obtain the optimal longitudinal current profile for a bunch propagating through a single bend in presence of steady-state and transient CSR, and for a 4-bend chicane as well, and described a numerical application to the benchmark chicane of the Berlin-Zeuthen CSR workshop of 2002. This type of longitudinal distribution is meant to be obtained using longitudinal laser shaping at the cathode or applying a longitudinal-transverse emittance exchange. Possible limitation: the maximum sustainable Twiss parameter variation along the bunch from the point of view of the optics matching in the undulator and the FEL efficiency. Another way to mitigate the induced emittance growth in case of strong bunch compression, has been indicated by [15] in the control and suppression of the current spikes, (current horns), forming at the head and tail of the compressed bunch, typically removed by means of collimators. They identified these current horns as caustics forming in the electron trajectories and presented a method to analytically determine the conditions to avoid the caustic formation. These conditions are met with the addition of optical elements such as sextupoles and octupoles within the bunch compressors to control the T_{566} and U_{5666} terms and move the compressor working point outside the condition that identifies the caustics formation. In other words, after passing through a chicane the final longitudinal position relative to the center of the bunch of any electron is:

$$z_f = z_i + R_{56}\delta + T_{566}\delta^2 + U_{5666}\delta^3 + \dots \tag{58}$$

where R_{56}, T_{566}, and U_{5666} are the first-, second- and third-order longitudinal dispersion respectively and δ is the relative energy deviation; given a set of these parameters the condition for the formation of a caustic at the end of a bunch compressor is:

$$R_{56}\delta'(z_i) + T_{566}\delta''(zi) + U_{5666}\delta'''(z_i) + 1 = 0 \tag{59}$$

where $\delta(z_i)$ is the shape of the initial longitudinal phase space or chirp, often described by a high order polynomial and $\delta'(z_i)$ is the derivative with respect to z_i. The parameter set of the compressor (R_{56}, T_{566}, U_{5666}) is a point that lies in the $[T_{566}, U_{5666}]$ plane where the caustics regions can be identified and the control of these parameters, by means of the addition of sextupoles and octupoles, can move the compressor working point in a free region determining a significative reduction of the transverse emittance dilution. It should also be mentioned the five-bend chicane bunch compressor proposed for LCLS-II [16]: the 5-bend chicane has several distinct features that distinguishes itself from the standard 4-bend chicane with regards to CSR induced emittance growth suppression. Firstly, the additional bend allows the ability to allocate the R_{56} amongst the five bends (the R_{56} of a 4-bend is predominantly constrained into the two middle magnets). This additional flexibility is likened to an optics-like tuning of the CSR energy kicks in each of the bending magnets. Additionally, the dual-polarity dispersion of the chicane opens the possibility of locally cancelling path/angle excursions caused by the CSR energy kicks. From the simulation studies reported in reference [16] and conducted for the present LCLS-II-HE 4-bend BC2 design and the proposed 5-bend BC2 chicane design, a significant reduction of the emittance dilution is obtained in all the considered cases.

Far from being exhaustive, this overview of the methods for the mitigation of the emittance dilution can be closed citing the paper by Yi Jiao et al [17] in which they provide generic conditions for suppressing the emittance growth in a two dipole achromat. It is not the case of a bunch compressor, but it is interesting from the point of view of a beam transport system with small momentum compaction and almost constant bunch length. They adopt a modified C-S formalism analysis with the respect to ref. [12] in which the CSR kick is linearized in

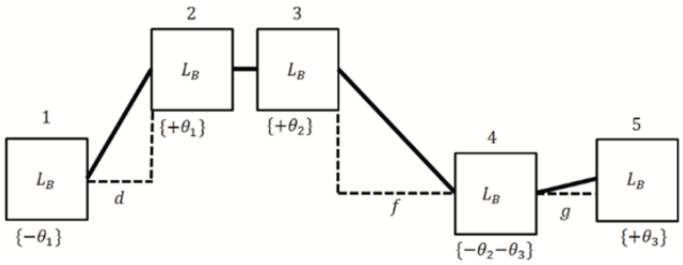

Figure 12: Diagram of a five-bend chicane [16]. Not to scale.

the limits of its validity, (i.e. bending angle from 1° to 12° and bending radius from 1 to 150 m), and inserted in the equation of motion as a contribution to the particle energy spread. The dipole R-matrix is then extended and used for the whole two dipole achromat matrix calculation. Through matrix manipulations the finally find the condition for the CSR cancellation in the single kick approximation of the CSR effect applicable also for a more generic case of an achromat consisting of three or more dipoles. With Elegant simulations they successfully verify the validity of the approach also in comparison with other methods as the optical balance mentioned above.

4 Preliminary RF design

4.1 X-band linearizer

In this section we discuss a preliminary (but complete) RF design of the X-band linearizer. For reader convenience, the specifications are summarized in the Table 6. The structure length depends on the available space while the (relatively) large iris radius allows a large acceptance needed for the expected beam transverse size. One has to remember that this structure may decelerate the beam, thus RF defocusing may occur.

Table 6: X-band linearizer design specifications

Design parameters		
Accelerating gradient	65	MV/m
Frequency	11.9952	GHz
Working mode	$2\pi/3$	
Length	0.6	m
Iris radius	4	mm

A first design option has been carefully studied, proposing a constant impedance travelling wave structure satisfying the Table 6 specifications; the constant cell size results in a decrease of the available accelerating gradient with respect to a constant gradient, but it allows a better physical aperture, useful for beam dynamics reasons.

In this section, we focus on the EM simulations results of the structure for two cases of single cell geometry. Then a brief analysis of breakdown phenomena follows to better understand the trade-off between complexity realization of the cell and breakdown probability.

According to Table 6 requirements, we first design the single cell of the structure. Two types of geometries have been considered, one is the simple circular iris cell, while the second one is the edge rounding elliptical cell, in order to minimize the modified Poynting vector and then reduce the breakdown probability of the structure, and maximize the shunt impedance [18]. Then couplers have been designed as well. All the simulations has been performed using CST Microwave Studio.

4.1.1 Single Cell design

The geometries of the single cell are shown in Fig. 13. The tuning of elliptical cell is aimed to minimize the ratio between the modified Poynting vector ($S_{c,max}$) and square of the accelerating field (E^2_{acc}) [19] with a proper choice of elliptical ratio r_1/r_2. $S_{c,max}/E^2_{acc}$ as a function of the elliptical ratio r_1/r_2. is shown in Fig. 14; the minimum value has been obtained for r_1/r_2=1.3.

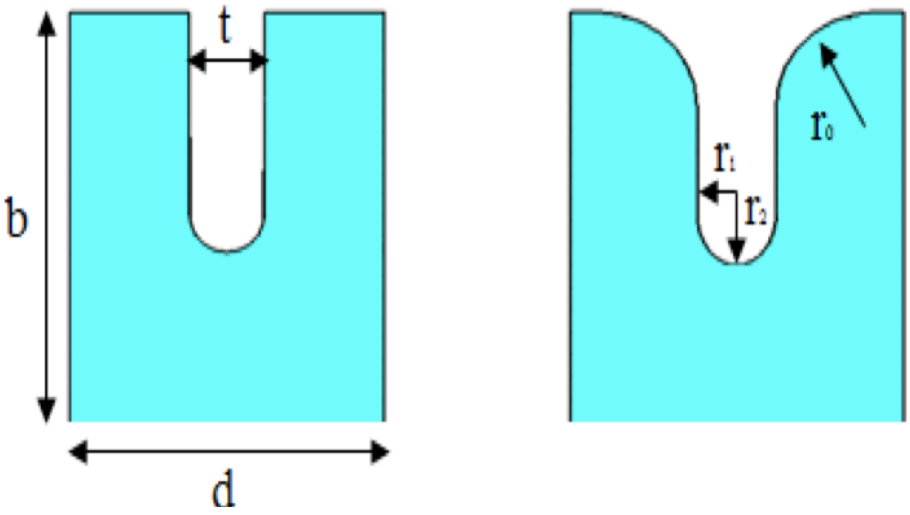

Figure 13: Geometry of the single cell.

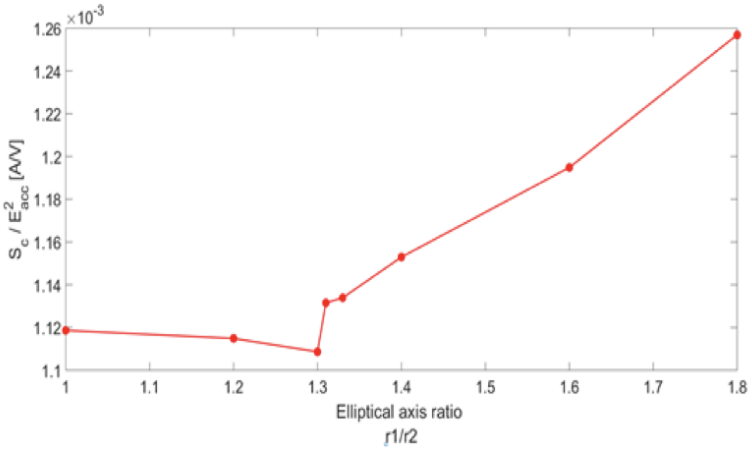

Figure 14: Modified Poynting vector as a function of elliptical ratio.

The main cells parameters are specified in Table 7 for the two design options. Each CST simulation has been performed with 1 Joule of energy stored in the single cell. In Fig. 15 module and phase of accelerating electric field are shown.

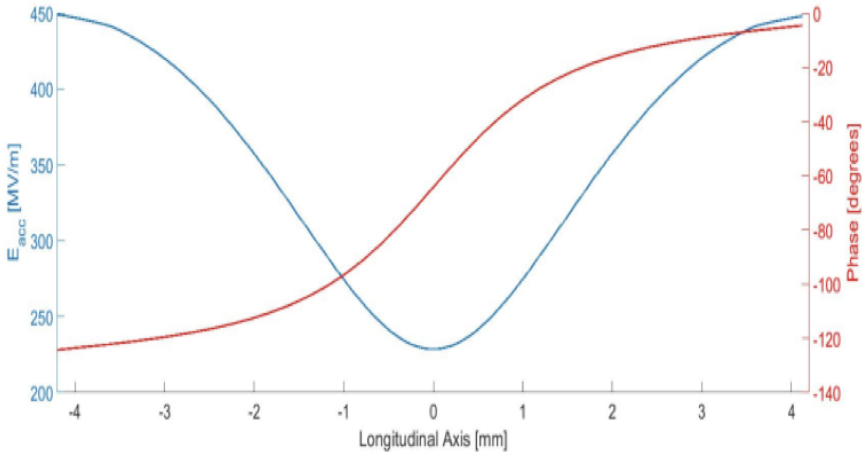

Figure 15: Phase and module of the single cell (elliptical cell case).

Table 7: Single Cell Parameters

	Circular	Elliptical
Iris radius [mm]	4	4
Iris thickness t [mm]	2	2
Elliptical ratio r_1/r_2		1.3
Edge rounding radius for the r_0 [mm]		2.5
Outer radius b [mm]	10	10
Cell length d [mm]	8.398	8.398
Shunt Impedance [MΩ/m]	87	96
v_g/c [%]	3.7	3.8
Filling time [ns]	0.76	0.73
Quality Factor	6550	7292
Modified Poynting Vector [MW/mm^2]	132.35	122.15

4.1.2 Coupler Design

A single fed z-type coupler has been chosen for both geometries cells because of its compactness with respect to the wave-guide and mode launcher ones [20]. Racetrack geometry has been implemented in order to compensate the residual quadrupole field components. The coupler tuning has been performed using short circuit method according with [21]. The coupler geometry is shown in Fig. 16.

To first order, the azimuthal magnetic field near to the longitudinal axis is given by:

$$B_\phi(r,\phi,z) \simeq A_0(z)r + \sum_{n=1}^{\infty} A_n(z)\cos(n\phi)r^{n-1} \tag{60}$$

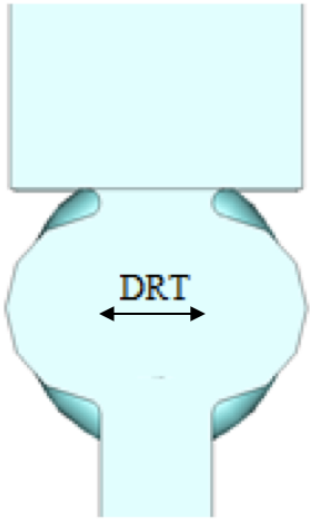

Figure 16: Coupler geometry. DRT parameter is indicated

In order to delete the quadrupole component, the term A_2 (gradient of quadrupole) must to be zero. The plot of this term, in the case of circular iris cell, as a function of the DRT parameter is shown in Fig. 17. The value of 0.1 has been obtained for DRT=9.5mm in the circular iris case and for DRT=10mm in the elliptical case. A comparison of the azimuthal magnetic field at 2mm from the longitudinal axis at the center of the coupler is shown in Fig. 18.

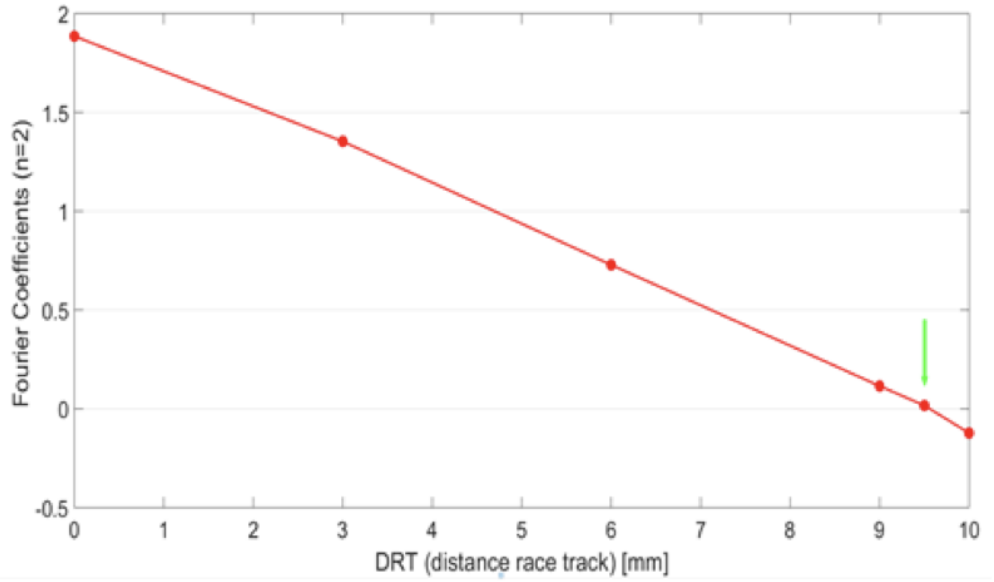

Figure 17: Quadrupole gradient as a function of distance race track (DRT).

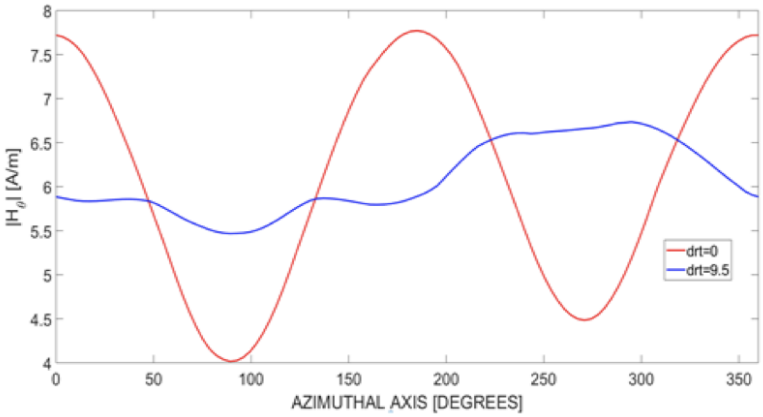

Figure 18: Modified Poynting vector as a function of elliptical ratio.

4.1.3 Full Structure EM Simulation and Breakdown Analysis

A module of accelerating electric field in the elliptical iris case is shown in Fig. 19. Simulations has been performed with 64 cells plus couplers according to length requirement. In both cases the reflection coefficient at the input port is below -30 dB. In Table 8, average accelerating gradient is shown for the corresponding input port power. The material chosen for simulations is copper annealed.

Table 8: Accelerating Field and Input Power for circular and elliptical single cell irises

	Average Accelerating Field [MV/m]	**Input Power [MW]**
Circular iris [mm]	64,5	33
Elliptical iris [mm]	63,3	30

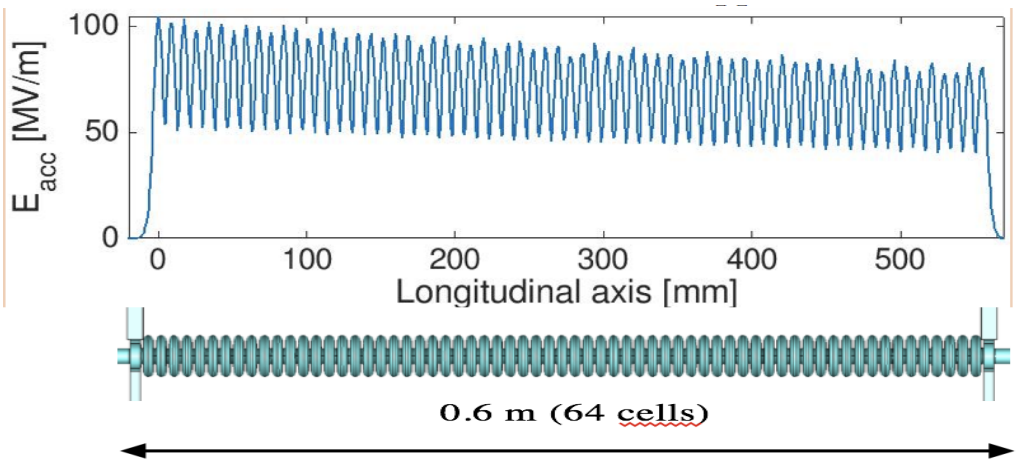

Figure 19: Accelerating field as a function of longitudinal axis.

The principal limitation Linac is the RF breakdown. In this work the main cause of this phenomena, RF pulsed heating, has been take into account. At first, an analysis of pulse

heating at the edge of the slots couplers has been done then using scaling law by Ref. [18] an estimation of BDR has been calculated.

The RF power flowing through the coupler slots generates a surface current flowing along the edges of the slots. Here the RF current reaches its maximum value. The temperature rise is given by

$$\Delta T[^{\circ}C] = 127 \left| H_{||}[MA/m^2] \right|^2 \sqrt{f_{RF}[GHz]} \sqrt{t_p[\mu s]} \tag{61}$$

If the temperature remains below 50°, damages in copper are practically avoided. If the temperature remains between 50° and 100° the breakdown probability increases. Over 100° breakdown occurs. Tangential magnetic field at the edges of the slot coupler is shown in Fig. 20. In both cases the maximum value is about 0,6 MA/m. The raise temperature as a function of pulse time square is shown in Fig. 21. In order to avoid coupler breakdown, a flat RF pulse of the duration below 77ns is needed. In our case the filling time of the structure is below 50ns, then using a RF pulse of this duration, breakdown in coupler can be avoided.

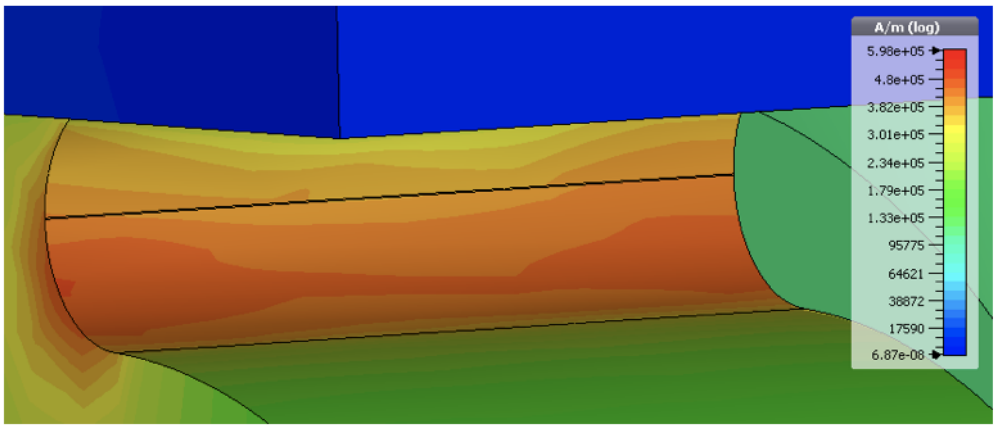

Figure 20: Tangential magnetic field at slot edge.

According to Ref. [18], it is possible to establish a dependence between modified Poynting vector, pulse duration and BDR given by:

$$\frac{S_c^{15} t_p^5}{BDR} = const. \tag{62}$$

BDR is defined as the probability to have a breakdown event and it is measured in breakdown per pulse per 1 meter of structure. For the new RF structures, S_c should not exceeds 4MW/mm^2 in order to obtain a BDR of 10^{-6} bpp/m for a 200ns pulse length. Using this scaling law it is possible to estimate the BDR for our cases. The results are shown in Table 9. As we expected the BDR in the elliptical case is smaller than in the circular iris case.

4.2 Ka-band linearizer

We present the design of a compact TW accelerating structure operating on the third harmonic with respect to the linac frequency (11.994 GHz option) with a 100-125MV/m accelerating gradient. Numerical electromagnetic simulations were carried out by using the numerical codes HFSS and CST.

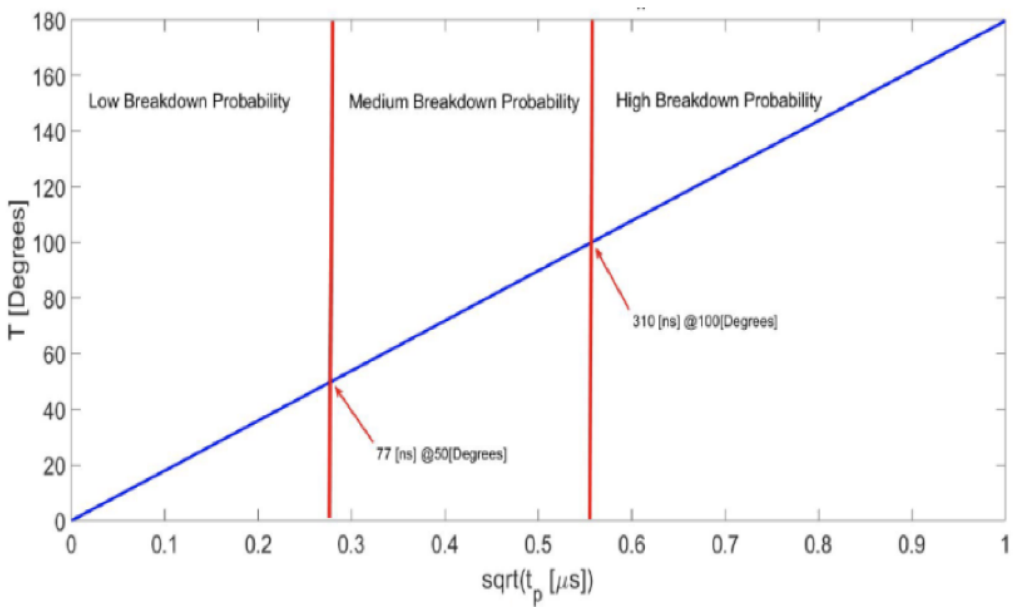

Figure 21: Temperature raise as a function of pulse time square.

Table 9: Temperature Raise and BDR for circular and elliptical irises

	Circular	**Elliptical**
Filling Time [ns]	48.64	46.72
H_{max} [MA/m]	0.64	0.63
Temperature [degrees]	40	38
Modified Poynting Vector [MW/mm^2]	6.78	5.83
Breakdown per pulse per meter [bpp/m]	2.33e-06	0.2e-06

The proposed structure is to be used in the linac working at 11.994GHz. In order to compensate the non-linearity distortions due to the RF curvature of the accelerating cavities, the use of a compact third harmonic accelerating structure working at 35.982 GHz is required citeEmma2001X-BandLCLS.

The analysis of the combined action of the Ka-band structure and the bunch compressor on the beam transport has been performed. Since only the single bunch operation is foreseen, the beam dynamics is not affected by the long-range wake-fields and no dedicated dampers of the parasitic higher order modes are adopted for the linearizer structure.

The technologies in the Ka-Band accelerating structures, high power sources and modulators have also been developed in order to reach a RF power output of 40-50MW by using the SLED system [22–24]. It has to be noted that this RF power level is more than it is needed for our proposed TW accelerating structure.

RF stability during operation and tuning tolerances are important points for the RF structure design in the high frequency range. The complexity of machining, tight mechanical tolerances and alignments are therefore important aspects which have to be taken into account in the design activity.

In order to obtain the longitudinal phase space linearization and from beam dynamics considerations in the framework of the Compact Light XLS project , we have designed a possible

compact high harmonic traveling wave (TW) accelerating structure operating at a frequency of 35.982GHz with a 100 MV/m accelerating gradient operating on the $2\pi/3$ mode.

This section is devoted to the choice of the fundamental RF parameters as the form factor to R_{sh}/Q, quality factor Q, power losses, dispersion curves, cooling system of a TW wave structure operating on $2\pi/3$ mode, with discussions on practicalÂ accelerating gradients.

4.2.1 Choice of the structure parameters

The design of the particle accelerators of new generation is defined on the basis of a compromise among several factors: RF parameters, beam dynamics, RF power sources, easy fabrication, small sensitivity to construction errors, economical reasons and so on. In order to minimize the input power requirements for a given accelerating gradient, the RF accelerating structures have to be designed with the aim of maximizing the shunt impedance. On the other hand, the accelerating section performances could be limited by effects such as the beam loading, instabilities, beam break-up etc., caused by the interaction between the beam and the sections.

As an example, a figure of merit for the accelerating structure is the efficiency with which it converts average input electromagnetic energy per unit length, into average accelerating gradient. Then, if P_b is the average beam power and the P_{rf} the average RF power fed into the structure, the small fraction of energy extracted by beam defined as well and $\varepsilon = P_b/P_{rf}$ has to be kept well below to some $\%$ for getting a satisfactory energy spread.

On the basis of these simple considerations, the global RF properties for designing the accelerating structure are therefore summarized and listed in the following:

- High accelerating field gradient to reduce the accelerator length;
- High shunt impedance to reduce the requirement of RF power;
- Low ratios E_p/E_0 and B_p/E_0, where E_p and B_p are the surface electric and magnetic peak fields respectively and E_0 is the average accelerating field, to achieve the highest possible field gradient before reaching the breakdown condition and to reduce thermal effects.
- High ratio E_0/W where W is the energy stored in the structure per unit length that is a measure of the efficiency with which the available energy is used for the operating mode;
- High group velocity in order to reduce the filling time of the section in order to get less sensitivity to the mechanical imperfections;
- Low content of longitudinal and transverse higher order modes which can be excited by the bunches traversing the structure and those can affect the beam dynamics;
- Appropriate shape profile for avoiding the generation of multipactoring phenomena which could limit the accelerating section performances.

Our concern is to design a constant impedance accelerating structure operating on the $2\pi/3$ mode with the requirements reported below:

- average accelerating field E = 100 MV/m;
- Axial length, L = 25 cm;

- beam aperture diameter, D = 2.66 mm;
- operating frequency, F = 35.982 GHz;
- ratio of phase to light velocity equal to 1;
- pulse charge, Q = 75 pC;
- rms bunch length pulse length, τ = 350fs
- single pulse operation
- pulse repetition rate frequency 1-10 Hz.

No specific effect due to the beam loading and beam dynamics has to be expected since the operation with a small average current and single bunch is adopted.

We decided to work in TW configuration in order to get a satisfactory longitudinal shunt impedance of the operating mode and an acceptable iris aperture for practical beam dynamics considerations. The third harmonic frequency of the main Linac one, implies small physical dimensions and thereby the dissipated power constitutes one of the main constraints, as well.

A reasonable upper limit on the average power dissipation has been estimated to be around at 4 kW/m. To meet the full requirements by keeping a flexibility margin, a section with simpler geometry which is cheap and of reliable construction and with satisfactory mechanical tolerances has been chosen. The detailed RF properties and the thermal behaviour of the $2\pi/3$ mode are described later in the following subsections.

4.2.2 Accelerating structure RF properties

In order to get a satisfactory longitudinal shunt impedance of the TM_{01} operating mode, we decided to work on the common $2\pi/3$ configuration mode of the TW structure with a cell-to-cell phase-shift of 120 degrees and by using the SLED system for obtaining the RF power source for feeding the structure.

In Fig. 22 we show the cell cavity shape of the for the $2\pi/3$ configuration mode on axis coupling through the iris aperture. The RF structure design study has been carried out by using the well-known HFSS and CST software.

Electric and Magnetic field distributions are illustrated in Fig. 23. The minimum value of the electric and maximum value of the magnetic fields are near the outer surface of the cavity as expected to be for the TM_{01} working mode.

In Figs. 24, 25, 26, we report the longitudinal shunt impedance, the unloaded quality factor and the cavity radius as function of the iris radius by keeping unchanged the operating frequency of the of the working mode TM_{010} at 35.982 GHz. With an iris radius of a = 1.333 mm, cavity radius b = 3.657 mm, thickness iris h = 0.667 mm, we are able to get a longitudinal shunt impedance R_{sh}/m = 158 $M\Omega/m$ and an unloaded quality factor Q = 4110.

Figure 27 shows the dispersion curve by giving the frequency mode as function of the phase advance of the TW structure. The group velocity of the $2\pi/3$ is estimated to be 0.0365 c. The energy spread due to the beam loading is negligible as it will be described in a forthcoming paper.

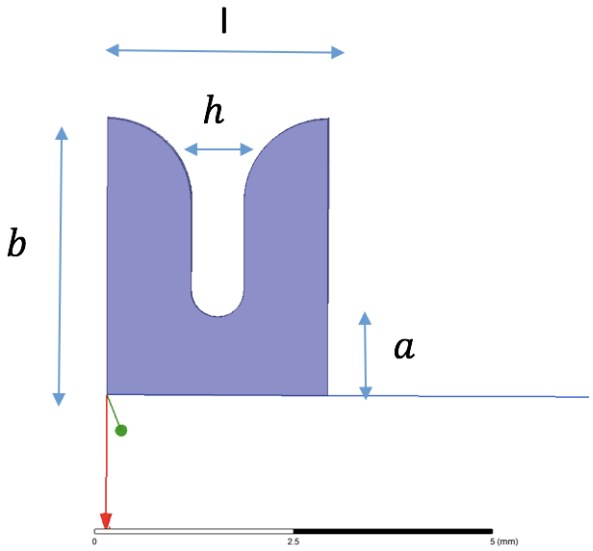

Figure 22: cavity shape of the TW $2\pi/3$ mode

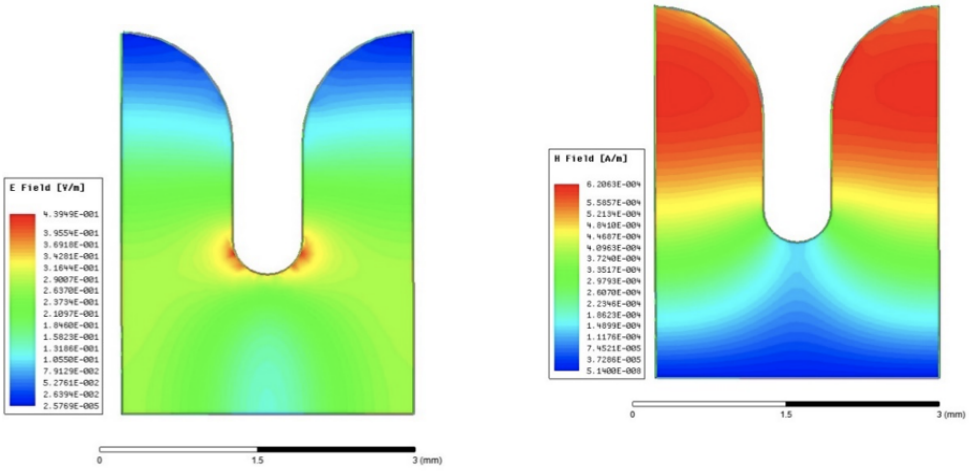

Figure 23: Electric field (left picture) and magnetic field (right picture) distribution of the TM_{010}

4.2.3 Breakdown rate (BDR) limit

The BDR limits the maximum accelerating gradient achievable inside the linac for a given RF pulse length and attenuation coefficient and τ.

The BDR measures the RF sparks per unit time and length inside an accelerating structure. Typical values, in the design of high-energy accelerators, are about $10^{-6} - 10^{-7}$.

A new quantity has been introduced [19], the modified Poynting vector defined as $S_c = re(S) + im(S)/6$ where S is the Poynting vector, in order to have a parameter to refer to during the linac design.

For the Ka-Band structure, we estimated a modified Poynting of $S_c \simeq 5$ MW$/mm^2$ (below safety threshold of about 6.3 MW/mm^2) for an accelerating gradient of E_{acc}=100 MV/m, input

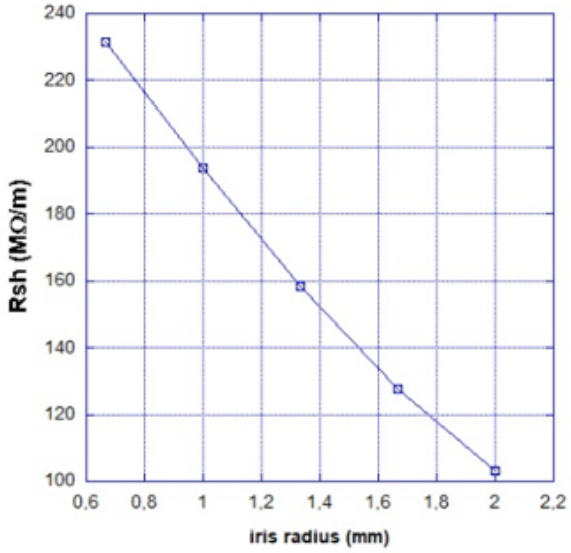

Figure 24: Shunt impedance as function iris aperture as function of the iris radius at 35.982GHz

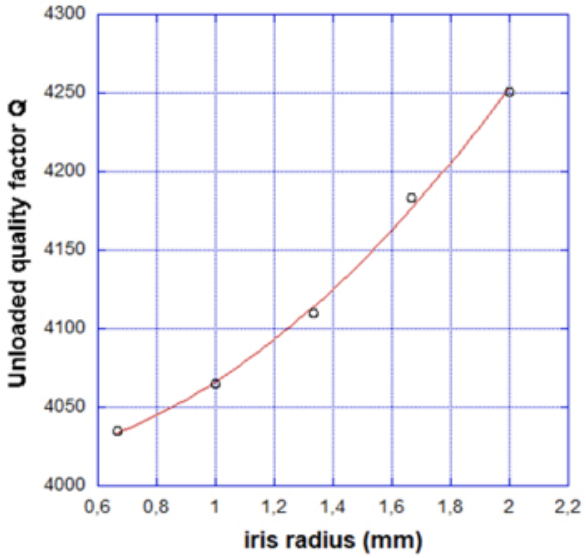

Figure 25: Unloaded quality factor as function of the iris radius at 35.982 GHz

power 25 MW, RF pulse length (flat top) 50 ns and an attenuation of τ= 0.57 Np.

The RF pulsed heating is estimated to be $\Delta T = 10.2deg$ below the safety threshold of $\Delta T = 50deg$. It is possible to increase the accelerating gradient Eacc up to 125 MV/m which gives a $S_c \simeq$8 MW/mm^2 that is somewhat more critical but near the threshold with a pulsed heating of $\Delta T = 16deg$ below the safety threshold.

For the lower energy and longer pulse case, in order to keep constant the BDR value, the

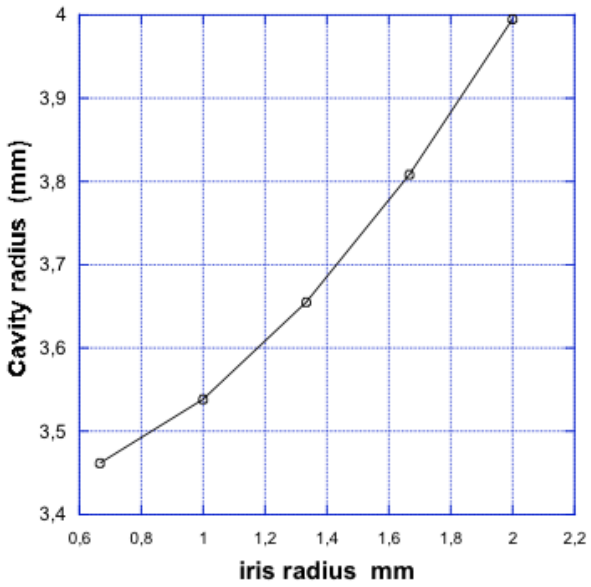

Figure 26: Cavity radius as function of the iris radius at 35.982 GHz

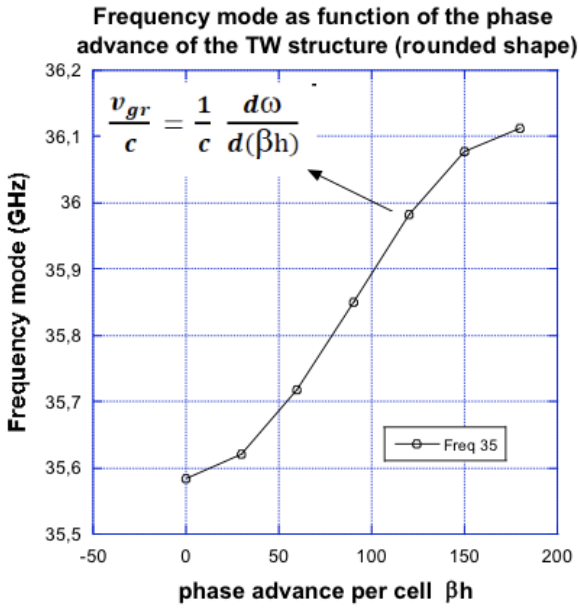

Figure 27: Dispersion relation of the TW structure

max accelerating gradient should not exceed 80 MV/m for a 1.5 μs pulse width.

The change of resonance frequency as function of cavity and iris radius have been estimated to be around $\Delta f = 11MHz/\mu m$ and $\Delta f = 5MHz/\mu m$, respectively. By adjusting the cavity radius and the iris radius in opposite directions, the corresponding frequency shift is estimated to be of 8 MHz/μm. To summarize, the cavity frequency shift per unit radius can be

expressed as

$$\sum_{i=1}^{i=2} = \left(\frac{\Delta f}{\Delta x}\right)_i = 6MHz/\mu m \tag{63}$$

(where i=1 refers to the cavity radius while i=2 to the iris radius adjustment), as it is expected to be. As a result, tuners devices and the temperature tuning approach have to be foreseen, too.

The performance of the accelerating structure may also be limited by the resonant electron discharges or multipactoring. According to our experience, it is well known that for reducing or eliminating this phenomenon it is recommended to have a curved profile of the cavity surfaces or to use asymmetric cavity shapes. Due to the big aperture of the structure, we believe that the two points multipactoring in the gap region of the structure is unlikely to occur since the counteraction of the radial electric force and magnetic force is uncompensated, thereby no resonant discharges can be determined. It is also well known the for reducing or eliminating the two points multipactoring it is recommended to use a rounded profile for the cavity shapes. Therefore we expect to have no particular problem for the multipactoring phenomenon.

4.2.4 Thermal and Stress Analysis

A rise in temperature will vary the accelerator dimensions and the frequency characteristic will change accordingly. The temperature rise can be reduced by means of a cooling system. For getting the frequency shift behaviour as a function of the temperature change, the thermal study is also required. We want to estimate the frequency shift caused by a change in temperature over the accelerating structure operating on $2\pi/3$ mode. We will assume that a closed cooling water system is used in order to keep the operating temperature at 40deg.

The preliminary thermal and stress analysis was also carried out in CST. In Fig. 28, we show the result of the single cell where a cooling system with longitudinal pipes is assumed. The simulation is performed assuming a gradient of E_{acc}=125 MV/m with a corresponding average power per unit length of about 2 kW/m, with a water flux of 3l/min. The hot spot is about 40deg (standard operation) and it can be lowered by adjusting water flux and water temperature. The consequent stress analysis shows a yield strength (Von Mises) < 20 MPa which is below the safety threshold for copper (70 MPa). The corresponding maximum displacement is about 1μm (i.e. frequency shift is negligible or tunable). The cooling system will be optimized during final engineering (water jacket or brazed channels) in order to avoid water-to-vacuum leaks.

It has been experimentally demonstrated that hard copper is able to stand ultra-high gradients unlike high-temperature treated one. As a result, we plan to machine the Ka-Band linac for high gradient applications in two halves with TIG welding of the outer surfaces. We are also considering an alternative approach as a novel clamping technique, as for medium-low energy range for the industrial/medical applications.

4.2.5 Ka-band linearizer main parameters

This structure can work with a high gradient accelerating up to 125 MV/m by using the conservative main RF parameters. We are planning to finalize the structure design as well as engineering of the RF power source that will be able to produce up to a (40-50) MW input power by using a SLED system.

In case of the single bunch operation, also a numerical and analytical study of the longitudinal and transverse wake-fields on the beam dynamic effects has been carried out and

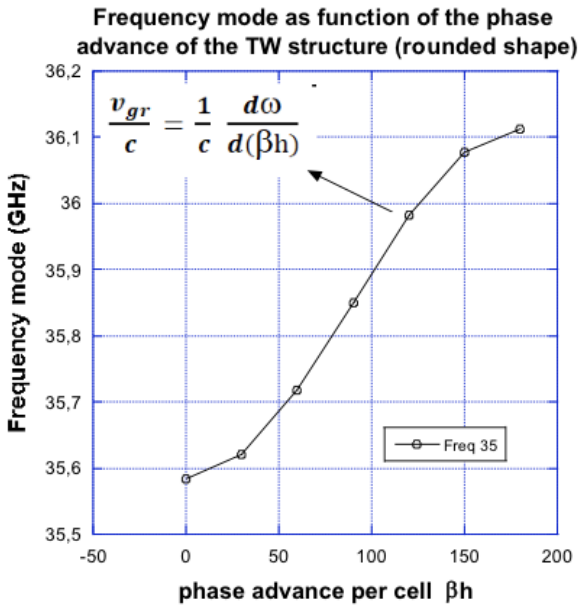

Figure 28: Thermal simulations of the single cell from CST software

discussed at first XLS Compact Annual meeting at Barcelona Spain. As a result, the estimate of the longitudinal and transverse wake-fields on the beam dynamic gave no specific trouble. The report on the wake-fields studies will be presented in a forthcoming paper.

As a final comment, the dimensions of the cavity are perfectly consistent with the 100 GHz structures by scaling law with the frequency already tested at SLAC.

The summary of the main RF parameters of the Ka Band constant impedance structure are reported in Table 10.

Table 10: Ka-band linearizer design specifications

Design parameters		
Frequency	35.982	GHz
Accelerating gradient	100	MV/m
Longitudinal shunt impedance	158	$M\Omega/m$
Unloaded quality factor	4110	
Cell length	2.779	mm
Structure length	250	mm
Group velocity/c	3.65	%
Input peak power	30	MW
Modified Poynting vector S_c	5	MW/mm^2
RF Pulsed heating	10	Celsius degree
Repetition rate	1-10	Hz
Power Source	25	MW

References

[1] P. Castro, *Beam Trajectory Calculations in Bunch Compressors of TTF2*, tech. rep., DESY, 2003, URL: https://bib-pubdb1.desy.de/record/138595.

[2] Y. Sun et al., *X -band rf driven free electron laser driver with optics linearization*, Physical Review Special Topics - Accelerators and Beams (2014), ISSN: 10984402, DOI: 10.1103/PhysRevSTAB.17.110703.

[3] S. Thorin et al., *BUNCH COMPRESSION BY LINEARISING ACHROMATS FOR THE MAX IV INJECTOR*, FEL2010, Malmö, Sweden, 2010.

[4] P. Craievich, *Passive longitudinal phase space linearizer*, Physical Review Special Topics - Accelerators and Beams (2010), ISSN: 10984402, DOI: 10.1103/PhysRevSTAB.13.034401.

[5] A. Latina, *Track1D*, Geneva, Switzerland, URL: https://gitlab.cern.ch/XLS-Git/WP6/tree/master/simulation_codes/beam_dynamics/Track1D.

[6] R. Talman, *Novel relativistic effect important in accelerators*, Physical Review Letters **56** (1986) 1429, ISSN: 00319007, DOI: 10.1103/PhysRevLett.56.1429.

[7] E. L. Saldin, E. A. Schneidmiller, M. V. Yurkov, *On the coherent radiation of an electron bunch moving in an arc of a circle*, Nuclear Instruments and Methods in Physics Research, Section A: Accelerators, Spectrometers, Detectors and Associated Equipment (1997), ISSN: 01689002, DOI: 10.1016/S0168-9002(97)00822-X.

[8] J. B. Murphy, S. Krinsky, R. L. Gluckstern, *Longitudinal Wakefield for an Electron Moving on a Circular Orbit*, Particle Accelerators (1997).

[9] P. Emma, R. Brinkmann, *Emittance dilution through coherent energy spread generation in bending systems*, 2002, DOI: 10.1109/pac.1997.750799.

[10] Douglas D., *Suppression and Enhancement of CSR-Driven Emittance Degradation in the IR-FEL Driver*, tech. rep., Thomas Jefferson National Laboratory, 1998.

[11] S. Di Mitri, M. Cornacchia, *Electron beam brightness in linac drivers for free-electron-lasers*, Physics Reports **539** (2014), ISSN: 03701573, DOI: 10.1016/j.physrep.2014.01.005.

[12] S. Di Mitri, M. Cornacchia, S. Spampinati, *Cancellation of coherent synchrotron radiation kicks with optics balance*, Physical Review Letters **110** (2013), ISSN: 00319007, DOI: 10.1103/PhysRevLett.110.014801.

[13] S. Di Mitri, *Feasibility study of a periodic arc compressor in the presence of coherent synchrotron radiation*, Nuclear Instruments and Methods in Physics Research, Section A: Accelerators, Spectrometers, Detectors and Associated Equipment **806** (2016), ISSN: 01689002, DOI: 10.1016/j.nima.2015.10.015.

[14] C. Mitchell, J. Qiang, P. Emma, *Longitudinal pulse shaping for the suppression of coherent synchrotron radiation-induced emittance growth*,
Physical Review Special Topics - Accelerators and Beams (2013), ISSN: 10984402,
DOI: 10.1103/PhysRevSTAB.16.060703.

[15] T. K. Charles et al.,
Current-horn suppression for reduced coherent-synchrotron-radiation-induced emittance growth in strong bunch compression,
Physical Review Accelerators and Beams (2017), ISSN: 24699888,
DOI: 10.1103/PhysRevAccelBeams.20.030705.

[16] R. T. O. Khan D. Z.,
An Emittance-Preservation Study of a Five-Bend Chicane for the LCLS-II HE beamline,
38th International Free Electron Laser Conference, Santa Fe, NM, USA, 2017, p. 301,
DOI: 10.18429/JACoW-FEL2017-TUP030, URL: http://accelconf.web.cern.ch/AccelConf/fel2017/papers/tup030.pdf.

[17] Y. Jiao et al., *Generic conditions for suppressing the coherent synchrotron radiation induced emittance growth in a two-dipole achromat*,
Physical Review Special Topics - Accelerators and Beams (2014), ISSN: 10984402,
DOI: 10.1103/PhysRevSTAB.17.060701.

[18] A. Grudiev, S. Calatroni, W. Wuensch,
New local field quantity describing the high gradient limit of accelerating structures,
Physical Review Special Topics - Accelerators and Beams (2009),
DOI: 10.1103/physrevstab.12.102001.

[19] K. N. Sjobak, A. Grudiev, E. Adli, *New Criterion for Shape Optimization of Normal-Conducting Accelerator Cells for High-Gradient Applications*,
Proceedings, 27th Linear Accelerator Conference, LINAC2014, 2014, MOPP028.

[20] M. Diomede et al.,
Preliminary RF design of an X-band linac for the EuPRAXIA at SPARC_LAB project,
Nuclear Instruments and Methods in Physics Research, Section A: Accelerators, Spectrometers, Detectors and Associated Equipment (2018), ISSN: 01689002,
DOI: 10.1016/j.nima.2018.01.032.

[21] D. Alesini et al., *Design of couplers for traveling wave RF structures using 3D electromagnetic codes in the frequency domain*,
Nuclear Instruments and Methods in Physics Research, Section A: Accelerators, Spectrometers, Detectors and Associated Equipment (2007), ISSN: 01689002,
DOI: 10.1016/j.nima.2007.06.045.

[22] O. A. Nezhevenko et al., *Commissioning of the 34-GHz, 45-MW pulsed magnicon*,
IEEE Transactions on Plasma Science (2004), ISSN: 00933813,
DOI: 10.1109/TPS.2004.830539.

[23] O. A. Nezhevenko et al., *Status of 34 GHZ, 45 MW pulsed magnicon*,
Proceedings of the IEEE Particle Accelerator Conference, 2005, ISBN: 0780388593,
DOI: 10.1109/PAC.2005.1590958.

[24] O. Nezhevenko et al., *Status of X-band pulsed magnicon project*, 2002,
DOI: 10.1109/pac.2001.986563.